Unravelling the Mechanisms that Drive the Performance of Photocatalytic Hydrogen Production

Sergio San Martín[ID], Maria J. Rivero[ID] and Inmaculada Ortiz *

Department of Chemical and Biomolecular Engineering, ETSIIT, University of Cantabria, Avda. de los Castros s/n, 39005 Santander, Spain; sergio.sanmartin@unican.es (S.S.M.); mariajose.rivero@unican.es (M.J.R.)
* Correspondence: inmaculada.ortiz@unican.es

check for updates

Abstract: The increasing interest and applications of photocatalysis, namely hydrogen production, artificial photosynthesis, and water remediation and disinfection, still face several drawbacks that prevent this technology from being fully implemented at the industrial level. The need to improve the performance of photocatalytic processes and extend their potential working under visible light has boosted the synthesis of new and more efficient semiconductor materials. Thus far, semiconductor–semiconductor heterojunction is the most remarkable alternative. Not only are the characteristics of the new materials relevant to the process performance, but also a deep understanding of the charge transfer mechanisms and the relationship with the process variables and nature of the semiconductors. However, there are several different charge transfer mechanisms responsible for the activity of the composites regardless the synthesis materials. In fact, different mechanisms can be carried out for the same junction. Focusing primarily on the photocatalytic generation of hydrogen, the objective of this review is to unravel the charge transfer mechanisms after the in-depth analyses of already reported literature and establish the guidelines for future research.

Keywords: semiconductor–semiconductor heterojunction; photocatalytic hydrogen production; direct Z-scheme; type II heterojunction; sensitization; charge transfer mechanism identification

1. Introduction

Semiconductor-based photocatalysis has attracted great attention in recent decades because of its potential to contribute to solve worldwide environmental and energy issues. Moreover, photocatalytic generation of hydrogen (H_2) appears to promote a renewable energy source and a water remediation process at the same time. The simultaneous reduction and oxidation of water is a complex multistep reaction involving four electrons and is an energy-intensive reaction. One of the alternatives to improve the performance of the photocatalytic process consists of using other compounds as sacrificial molecules to act as electron donors, providing electrons for proton reduction. The most common substrates for photocatalytic hydrogen production are methanol, ethanol, triethanolamine (TEOA), and Na_2S/Na_2SO_3 [1–6]. The photocatalytic reaction involves three sequential processes: (i) absorption of photons with energy equal to or greater than the bandgap of the semiconductor, exciting electrons from the valence band (VB) to the conduction band (CB) and creating electron (e^-)/hole (h^+) pairs; (ii) separation of carriers and migration to active sites; and (iii) initiation of redox reactions [7–9].

Nevertheless, the solar-to-hydrogen conversion efficiency of typical photocatalysts is still low due to several drawbacks. (1) Recombination of the photo-generated electron/hole pairs. Electrons tend to fall from the CB to the VB very quickly, reducing carrier concentrations back to the equilibrium and releasing energy in form of unproductive heat or photons. (2) Trapping of electrons in shallow energy levels near the band edge, avoiding their participation in redox reactions. (3) Fast backward and side reactions (i.e., water can also be oxidized to form hydroxyl radicals or hydrogen peroxide). (4) Inability

to use visible light. Band gap of the most commonly employed semiconductors such as TiO_2 or ZnO is about 3.2 eV and thus, only UV light can be used for hydrogen production. Furthermore, UV light only accounts for 4% of the solar radiation while visible light share is around 50%. Thus, this inability to utilize visible light limits the efficiency of the solar photocatalytic reaction [9,10].

Since the development of a competitive technology is strongly dependent on the enhancement of photocatalytic activity, the above-mentioned issues have been addressed by exploring and developing new photocatalytic materials. The first use of semiconductors as heterogeneous photocatalysts for hydrogen production goes back to 1972, when Fujishima and Honda reported photocatalytic water splitting using TiO_2 as the photocatalyst [11]. Later on in 1977, homogeneous systems were also reported [4]. These systems typically included an organometallic complex as the catalyst and another organic compound as the photosensitizer. In the past decade, hybrid systems including organic catalysts and semiconductor materials as photosensitizers have also been tested [4].

In the case of heterogeneous photocatalysts, an outstanding evolution from the first TiO_2-based catalyst to the nowadays advanced composites has taken place. First, noble metal doping (Pt, Au, Ag, Pd, Rh, Ni, and Cu) and transition metal doping have been reported to be very effective for the enhancement of photocatalytic performance, extending the spectral response to the visible region [12–16]. However, transition metals may also act as recombination sites. Transition metals have also been found to cause thermal instability. With the aim to extend the response of the photocatalysts to the visible region, dye sensitization has been widely reported. Under visible illumination, the dye transfers an electron to the photocatalyst, promoting hydrogen production [10,17–20].

Synthesis of semiconductor–semiconductor heterojunctions (i.e., TiO_2/g-C_3N_4 [21], TiO_2/CdS [22], ZnO/g-C_3N_4 [23], TiO_2-WO_3 [24–26] or g-C_3N_4/$BiVO_4$ [27]) is another recent approach, which is a facile method with very promising results. The most remarkable features is that they contribute to avoiding charge recombination and coupling the properties of both semiconductors. Additionally, a more efficient catalyst with widened light absorption spectrum is obtained. This topic has been addressed in several review works such as Wang et al. [28], Moniz et al. [29], Yang et al. [30], and Fajrina et al. [31], who reported the synthesis and properties of different semiconductor–semiconductor heterojunctions. Moreover, Kandi et al. [32] and Rao et al. [33] gathered several references about the exceptional properties of using quantum dots to boost photocatalytic activity where the authors highlighted the quantum confinement effect of emitting multiple electrons, size-adjustable properties such as light absorption, and the benefits of quantum dot-semiconductor heterojunctions, especially in hydrogen production [34].

Zhao et al. [35] and Ong et al. [36] outlined g-C_3N_4-based heterojunctions due to the unique properties of carbon nitride mainly because it is an abundant material, but in also thanks to its visible light photocatalytic activity, robustness, and physicochemical stability. Zheng et al. [37] reported TiO_2-metal sulfide heterostructures, emphasizing the enhanced capacity in light harvesting, and also underlined the effectiveness of MoS_2 as a co-catalyst in photocatalytic hydrogen production.

The promising results obtained so far with semiconductor–semiconductor heterojunctions motivate discerning the charge transfer mechanisms responsible for the enhanced performance in order to drive the design of more efficient processes for photocatalytic hydrogen generation. However, there is still a great uncertainty about the mechanisms. Thus, this work is intended to advance the knowledge on the relationship between the experimental characterization of the photocatalysts' performance and the charge transfer mechanisms. Therefore, a critical review and analysis of the reported literature has been undertaken. Although this work is mainly focused on photocatalytic hydrogen generation, when necessary, other motivated applications have been also considered.

2. Charge Transfer Mechanisms: Concept and Relevance in Photocatalysis

Identifying the charge transfer mechanism and establishing the relationship with the photocatalyst nature and properties are key for the optimum design of photocatalytic processes; in fact, this is an important issue that is currently receiving great attention by the scientific community. This section

summarizes the main mechanisms that result from the combination and subsequent formation of two semiconductor heterojunction. Figure 1 gathers the band structure of the most outstanding photocatalysts [38] and clearly reflects that some of the semiconductors are only sensitive to UV light. Thus, it is interesting to couple them with other semiconductors that are able to absorb visible light with the aim of extending light absorption.
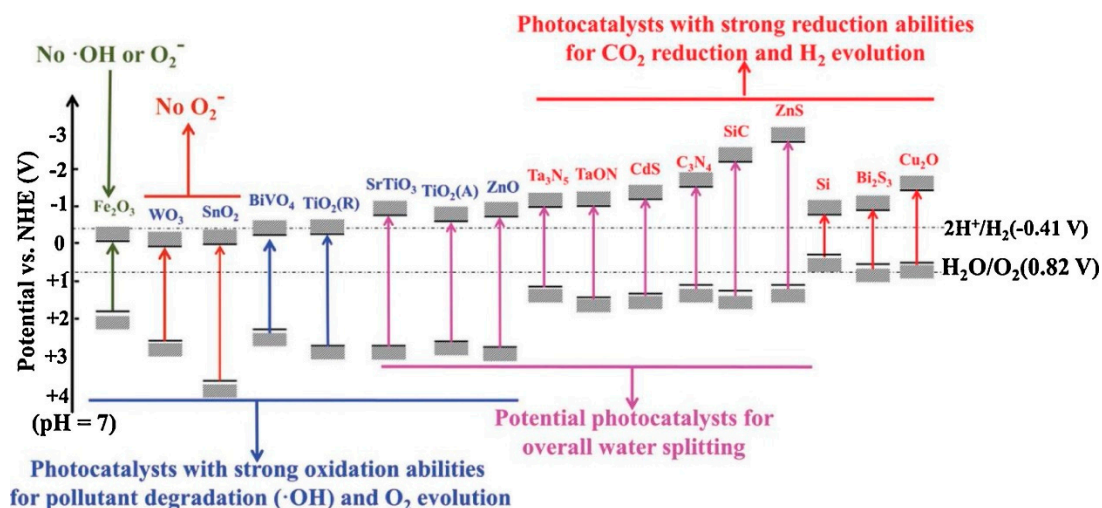
Figure 1. Band structure and potential application of various semiconductors. Reprinted from reference [38]. Copyright 2018 Elsevier.

Another aspect that needs further improvement refers to avoiding electron/hole pair recombination. With this objective, two semiconductors can be joined in a way where one of them acts as an electron sink and the second one as a hole sink.

According to energy band positioning, semiconductor heterojunctions are generally classified into three types: type I (straddling band gap), in which the conduction band (CB) of SCI is higher than the CB of SCII, whereas the VB from SCI is lower than VB from SCII (Figure 2A), so charges move from SCI to SCII; type II (staggered band gap), in which the conduction band of SCII is below the CB of SCI, thus acting as an electron sink, and the valence band of SCI is above the valence band of SCII and acts as a hole sink (Figure 2B); and type III (broken band gap), in which the CB of SCII is below the VB of SCI (Figure 2C), thus holes are transferred to SCII and protons can be reduced on both semiconductors.
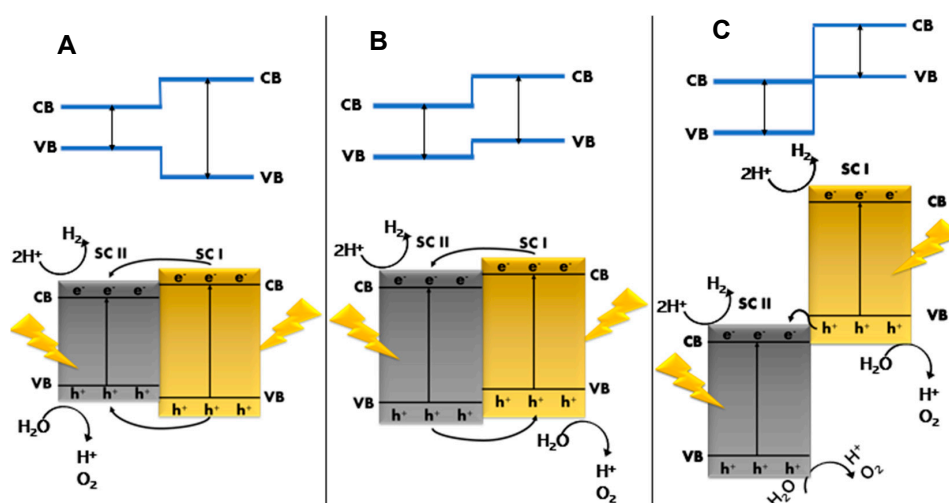
Figure 2. Classification of semiconductor heterostructures according to band position: (**A**) type I heterojunction; (**B**) type II heterojunction; (**C**) type III heterojunction.

However, only type II heterojunction can significantly promote the fast spatial separation of electrons and holes [38,39]. Therefore, the most common heterojunction proposed by researchers consists of two semiconductors with a staggered band structure. This leads to the formation of the heterostructure shown in Figure 3A. Moreover, according to the charge transfer mechanism and depending on whether both semiconductors or only one of them are activated by light, three charge transfer mechanisms can be proposed: sensitization (Figure 3B), type II heterojunction (Figure 3C), and the direct Z-scheme (Figure 3D) [7,30,40]
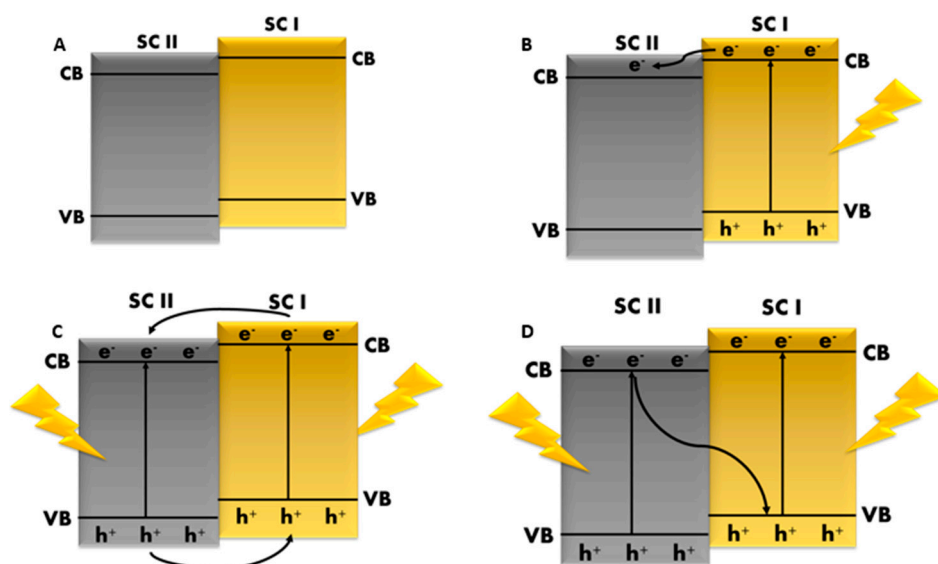
Figure 3. (**A**) Band structure of the SC–SC heterojunction. (**B**) Sensitization mechanism. (**C**) Type II heterojunction. (**D**) Direct Z-scheme.

In the sensitization mechanism, only one semiconductor is excited by incident light. Then, the photo-generated electron migrates from SCI with a higher conduction band (CB) position to SCII, which has a lower CB position. This mechanism proceeds when the light energy is not enough to promote electrons in both semiconductors. Generally, SCI can be activated by visible light, whereas SCII cannot. Therefore, it promotes spatial separation, thus reducing charge recombination. The sensitization mechanism with different semiconductors has been widely reported. One of the first methods for visible-light activation of photocatalysts was the modification by the physical deposition of Cr^{3+}, a transition metal ion, on TiO_2/RuO_2 composite to produce hydrogen under visible light [41]. However, some problems such as photogenerated charge recombination and blocking of surface active sites still remained [7]. Yu et al. [42] reported the synthesis of carbon quantum dots with sensitized TiO_2 with broader photo-response (extended light absorption) and enhanced hydrogen production compared to bare TiO_2. The sensitizing effect of the carbon quantum dots has been supported by other authors such as Zhang et al. [43] and Sargin et al. [44]. Wang et al. [45] developed sensitized SiC–g-C_3N_4 composites with high stability and superior hydrogen production than individual g-C_3N_4 or SiC photocatalysts.

When both semiconductors are excited by incident light, the type II heterojunction mechanism usually takes place, as shown in Figure 3C [46]. Since the energy of the CB of SCI is higher than the CB of SCII, the photogenerated electrons will migrate from SCI to SCII due to band alignment. Meanwhile, the photogenerated holes in the VB of SCII will move to the VB of SCI. Therefore, SCI acts as a hole sink and SCII as an electron sink. Therefore, spatial charge separation is promoted, and the photocatalytic activity and efficiency are enhanced. Nevertheless, this configuration may fail to drive some catalytic reactions as a result of the weakening of the redox capacity, since the lower the band energy, the lower the redox potential [46–48]. The type II heterojunction is a very well-known mechanism since the first mention of this band alignment goes back to the 80s with Ge_xSi_{1-x}/Si heterostructures [49]. It is the most common mechanism when TiO_2 and CdS are in contact [21,50–52]. However, Zhang et al. [52]

reported low photocatalytic degradation of pollutant activity with the TiO_2/CdS composite following type II heterojunction due to the appearance of photo-corrosion and the reduction of redox capacity of the composite photocatalyst during pollutant degradation. On the other hand, Liu et al. reported that the type II heterojunction mechanism was responsible for the photocatalytic hydrogen production with core-shell Cu_2O–g-C_3N_4 composites, giving a hydrogen production four times higher than pure Cu_2O [53].

In the direct Z-scheme mechanism (Figure 3D), the relative band alignment is similar to type II heterojunction and resembles the natural photosynthesis mechanism. When excited by incident light, the photogenerated electrons in SCI and the photogenerated holes in SCII remain in their respective bands, preserving the strong reduction and oxidation activity of the components. Meanwhile, the photogenerated electrons on SCII with a lower reduction potential than the electrons in SCI and holes on SCI with a lower oxidation potential than the holes in SCII recombine. As a result, the junction simultaneously has the strong redox capacity of both semiconductors and the reductive and oxidative sites are spatially separated, as reported in the reviews of Xu et al. [46], Low et al. [48], and Xia et al. [54] regarding direct Z-scheme composites for hydrogen production and dye degradation, respectively, and the review of Fu et al. 2018 [40] on g-C_3N_4 heterostructures. The Z-scheme concept was first proposed by Bard et al. in 1979 [55]. In this mechanism, two semiconductors are coupled by a shuttle redox mediator, commonly Fe^{3+}/Fe^{2+} and IO_3^-/I^- ion pairs. Sayama et al. in 2002 achieved excellent activity of Pt–$SrTiO_3$/Pt–WO_3 under visible light using IO_3^-/I^- as a redox mediator for water splitting [56]. Nevertheless, several drawbacks like slow rate and back reaction have led to the development of the all-solid-state Z-scheme, first reported by Tada et al. in 2006 for CdS and TiO_2 linked by Au as the electron conductor [57]. Although solid conductors performed better than the aforementioned ion redox pairs, the high price of the carriers and shielding effect of the nanoparticles have focused the attention of further researchers. Therefore, the direct Z-scheme concept was first proposed by Yu et al. in 2013 [58] when they fabricated g-C_3N_4–TiO_2 composites for formaldehyde degradation. Later on, Jiang et al. [21] reported the successful fabrication of TiO_2–CdS composites by selective deposition of CdS on TiO_2, achieving an enhanced hydrogen production. They also described a more stable catalyst that improved seven-fold hydrogen production compared to bare components. Recently, new catalysts like Nb_2O_5/g-C_3N_4, synthetized by Idrees et al. [59], have been proven to follow the direct Z-scheme mechanism, leading to increased hydrogen production compared to individual Nb_2O_5 and g-C_3N_4. Several works have been published providing information on identification techniques and the advantages of this mechanism on the performance of the photocatalysts. Worth mentioning are the works of Low et al. [48] and Xu et al. [46] regarding direct Z-scheme semiconductor heterostructures, or the report by Fu et al. that reviewed direct Z-scheme g-C_3N_4-based heterostructures [40]. Di et al. gathered metal sulfide direct Z-scheme heterostructures [60]. Kumar et al. studied zinc oxide-based heterojunctions, emphasizing the benefits of the direct Z-scheme mechanism [61].

It is remarkable that even the same materials can lead to different mechanisms depending on their synthesis procedure. For instance, Zhang et al. reported that when CdS was selectively deposited on the {001} facet of TiO_2, the composite behavior was type II heterojunction, but when the deposition was on a different facet ({101}), the proposed was direct Z-scheme [52]. Jiang et al. synthesized TiO_2/CdS through photodeposition, resulting in the direct Z-scheme while random, non-controlled chemical deposition resulted in the type II heterojunction [21].

Other mechanisms that have been explored in the literature are the semiconductor–metal junction (Schottky junction) (Figure 4A); p–n heterojunction (Figure 4B); and S-type heterojunction (Figure 4C).
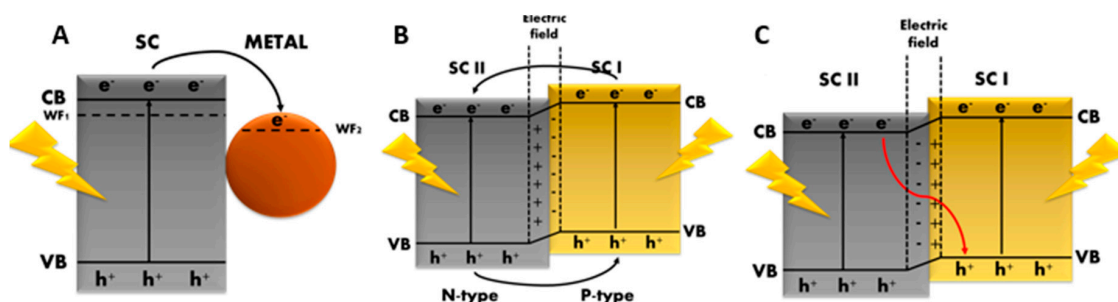
Figure 4. (**A**) Schottky junction. (**B**) P–n heterojunction. (**C**) S-type heterojunction.

In the Schottky junction, the dopant metal with a higher work function acts as a photogenerated electron sink, promoting charge separation in agreement with different works on heterogeneous photocatalysis such as Schneider et al. [2], Corredor et al. [4], Yang et al. [30], and Ribao et al. [62].

The p–n heterojunction is similar to the type II heterojunction. However, the formation of a built-in electric field improves and speeds up charge separation, as reported by Etacheri et al. [7], Wang et al. [28], Yang et al. [30], and Capilli et al. [63]. Nevertheless, it is very difficult to obtain experimental evidence supporting the difference between both mechanisms. In fact, some authors consider the p–n heterojunction as a class of type II heterojunction such as in Li et al. [38]. Hence, this report will use the term type II heterojunction to refer to the type II heterojunction and p–n heterojunction indistinctly.

The most recent charge transfer mechanism is the S-type heterojunction (Figure 4C), first proposed in 2019 by Fu et al. regarding WO_3/g-C_3N_4 composites for hydrogen production. S-type heterojunction is formed by the coupling of two n-type semiconductors. The driving force of the charge carrier transfer comes from the internal electric field between both semiconductors. Usually, the oxidation photocatalyst has a greater work function and lower Fermi level; in contrast, the reduction photocatalyst has a smaller work function and higher Fermi level. When the semiconductors are in contact, an internal electric field will be built and its direction is from the reduction photocatalyst to the oxidation photocatalyst [64]. However, this mechanism was be deeply considered in this report due to the limited information available.

In order to go one step further, in this work, the main experimental evidence to support the different charge transfer mechanisms were critically reviewed and analyzed, thus helping in the design of the photocatalytic process.

3. Charge Transfer Mechanisms: Supporting Experimental Evidence

Understanding the charge transfer mechanisms in photocatalysis, and more specifically in photocatalytic hydrogen generation is essential for process modeling, design, and optimization. In this section, the experimental techniques that provide information to discriminate the charge transfer mechanism are reviewed.

Charge Recombination. Charge recombination is one of the major drawbacks in photocatalysis. Semiconductor–semiconductor heterojunction is one of the proposed solutions to avoid it. Therefore, it is necessary to find out if the junction reduces recombination. Photoluminescence spectroscopy (PL) is an effective method that has been widely used in the literature [21,23,42,44,52,59,65–78]. Photoluminescence occurs when an electron moves from an excited state to a ground state. Hence, PL intensity can be directly proportional to the separation of photo-induced charge carriers: the stronger the PL signal, the higher the recombination of photo-induced carriers. A deeper explanation can be found in the photoluminescence study performed by Fujihara et al. [79] and the PL study of different semiconductors reported in the review by Liqiang et al. [80]. In these works, the spectra of the pure components and the composite photocatalyst were analyzed. A lower photoluminescence of the composite compared to that of pure components would be indicative of a lower recombination. Figure 5 shows the reduction of the PL of TiO_2/g-C_3N_4 when the content of TiO_2 increased, indicating

a synergistic effect of the heterojunction, leading to a lower charge recombination. It is remarkable to notice that, when g-C$_3$N$_4$ acted as the main component of the junction and its composition was over 30%, the PL spectra of the composite showed similar emission peaks to g-C$_3$N$_4$ (Figure 5A), whereas when TiO$_2$ acted as the main component, composite peaks were similar to those of TiO$_2$ (Figure 5B) [78].
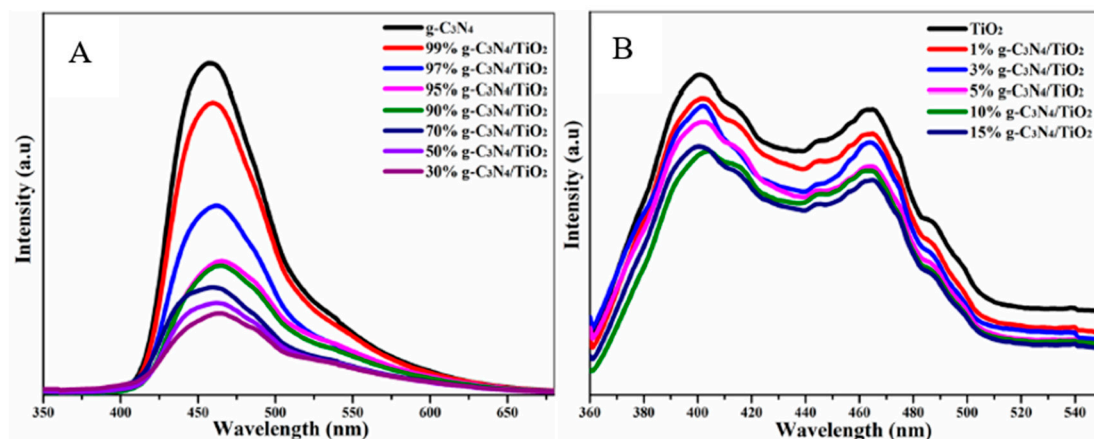
Figure 5. Photoluminescence spectroscopy emission spectra of (**A**) g-C$_3$N$_4$ and g-C$_3$N$_4$/TiO$_2$ and (**B**) TiO$_2$ and g-C$_3$N$_4$/TiO$_2$ composites under an excitation wavelength of 310 nm. Reprinted from reference [74]. Copyright 2020 ACS.

Band Gap and Band Structure Determination. Band gap is a defining property related to the excitation wavelength of semiconductors and composites. Diffuse reflectance spectroscopy is a standard technique for the determination of the absorption coefficient of the semiconductor as a function of the wavelength. Then, different researchers have made use of well-known methods to determine the band gap, like the Kubelka–Munk equation [81,82] (i.e., in Jo et al. and Liu et al. [67,83]), to determine the TiO$_2$/g-C$_3$N$_4$ band gap. The Kubelka–Munk equation has been widely used for an extensive number of composites (Fe$_2$O$_3$/g-C$_3$N$_4$ [21], TiO$_2$/CdS [21], CdS/g-C$_3$N$_4$ [72], TiO$_2$/g-C$_3$N$_4$ [83]). The Kubelka–Munk equation is usually represented through the Tauc plot, shown in the insert of Figure 6.
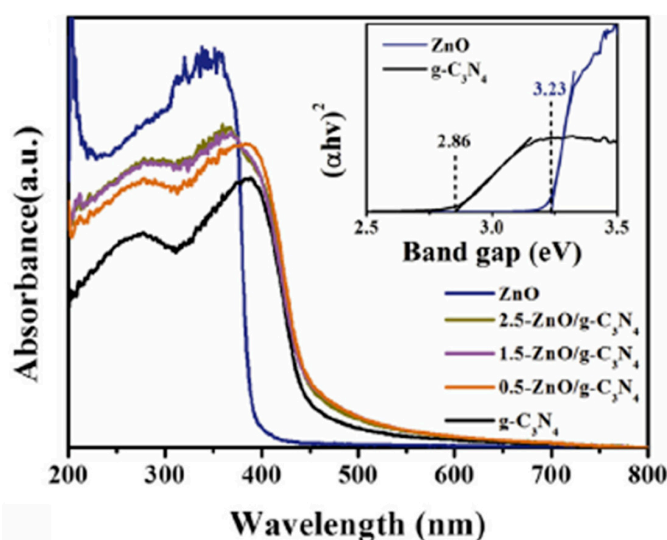
Figure 6. UV–Vis absorption spectra of ZnO, g-C$_3$N$_4$, and ZnO/g-C$_3$N$_4$ samples with different ZnO content. The insert spectrum is the Tauc plots of ZnO and g-C$_3$N$_4$. Reprinted from reference [23], Copyright 2019 Elsevier.

The band structure can be determined using empirical equations (Equations (1) and (2)) based on the electronegativity of the semiconductors (χ), the energy of the free electrons on the hydrogen scale (E^C), and the band gap energy of the semiconductor (E_g) [84,85].

$$E_{VB} = \chi - E^c + 0.5 * E_g \tag{1}$$

$$E_{CB} = E_{VB} - E_g \tag{2}$$

These equations have been used by Huang et al. [68], Wang et al. [71], and Wang et al. [77] in TiO$_2$/g-C$_3$N$_4$ composites and Wang et al. in SiC/g-C$_3$N$_4$ or Shang et al. for g-C$_3$N$_4$/Ag$_2$CrO$_4$ composites [86]. X-ray photoelectron spectroscopy (XPS) is also used to determine the band positions of semiconductors. Commonly, Mott–Schottky plots help to determine the Fermi level and the XPS provides information about the distance between the Fermi level and the valence band. With this information and the band gap, the conduction band can be also determined. This method was developed for ZnO/g-C$_3$N$_4$ in Wu et al. [23] and for CdS/g-C$_3$N$_4$ in Jiang et al. [72]. Ultraviolet photoelectron spectroscopy (UPS) is performed to detect the VB electronic structure information, thereby obtaining the VB position of a semiconductor. Along with the band gap, CB can also be determined. Some examples of photocatalysts that have been analyzed in this way are g-C$_3$N$_4$/BiVO$_4$ [27] or TiO$_2$ [87]. Computational calculations, as first-principles density functional theory (DFT), can provide insight into the coupling interactions and electron transfer at the interface of the heterostructure. These simulations are applied to determine highest occupied molecular orbital (HOMO) and lowest unoccupied molecular orbital (LUMO) states of uncoupled and coupled semiconductors. DFT is also able to ascertain the existence of internal electric fields [36,88,89].

Radical Species Trapping. Radical generation depends on the redox potential of the photocatalyst. Hence, radical generation will depend on band alignment, as shown in Figure 2. By confirming the existence of several radicals, the electron and hole sites can be confirmed indirectly. For instance, usually only the highest CB of the heterostructure has the energy to reach superoxide radical reduction potential (−0.33 eV vs. NHE), while only the lowest VB of the composite has enough energy to reach hydroxyl radical oxidation potential (+2.4 eV vs. NHE), thus confirming the direct Z-scheme. To trap radicals, several techniques have been detailed such as the ones described by Fernández-Castro et al. [90] and further developed by Ribao et al. to detect reactive oxygen species, ROS, on the activity of metal doped TiO$_2$ [91]. The radical trapping method measures the presence of hydroxyl radicals ($\bullet$OH), superoxide radicals (O$_2$$^-$$\bullet$), and holes (h$^+$) in photocatalytic degradation of dichloroacetic acid (DCA) by adding benzoquinone (BQ) as an O$_2$$^-$$\bullet$ scavenger, tert-butyl alcohol (t-BuOH) as a hydroxyl scavenger, and formic acid (FA) as a hole scavenger. The role of radicals is associated with the reduction in the photocatalytic activity after the addition of the specific scavenger. In that work, no inhibition was observed when O$_2$$^-$$\bullet$ radicals were removed by BQ, indicating that these species did not participate in the photocatalytic degradation process. However, when t-BuOH or FA were added to the DCA solution, total inhibition was observed, demonstrating that both holes and hydroxyl radicals play an important role in the DCA degradation process. Table 1 presents some of the scavengers used for each reactive species.

Electron paramagnetic resonance (EPR or ESR) has proven to be a powerful tool for the detection of ROS. Radical species have a very short life. Therefore, to obtain evidence of their presence, scavengers are required. For example, hydroxyl radicals have been quantified by dimethylsulfoxide (DMSO) [24,99]. In the work of Dvóranova et al. [100], ROS species produced by the photo illumination of TiO$_2$ were determined through this technique using DMPO (5,5-Dimethyl-1-pyrroline N-oxide), EMPO (5-(Ethoxycarbonyl)-5-methyl-1-Pyrroline-N-Oxide), and DIPPMPO (5-Diisopropoxyphosphoryl-5-methyl-1-pyrroline-N-oxide) as spin traps. Radical species are unstable but when they react with spin agents, they can be trapped and stabilized. More recent studies like those of Yuan et al. [78] and Ye et al. [69] also used DMPO to detect radicals responsible for the photocatalytic activity of TiO$_2$/g-C$_3$N$_4$ and CoTiO$_3$/g-C$_3$N$_4$/Pt composites, respectively. Figure 7 shows the detection

of hydroxyl radicals (Figure 7A) and superoxide radicals (Figure 7B) produced by TiO_2/g-C_3N_4 through ESR using DMPO as a spin trap.

Table 1. Scavengers used in the reviewed articles for each reactive species.

Reactive Species	Scavenger	References
$\bullet OH$	Tert-butyl alcohol	[23,70,91,92]
	Isopropanol	[21,52,67,68,83,93–95]
	Coumarin	[89,96,97]
	Terephthalic acid	[98]
$O_2^-\bullet$	Benzoquinone	[21,23,67,68,91,93–95]
	TEMPO	[52,83]
	Potassium bromate	[70]
	Argon	[92]
h^+	Formic acid	[91]
	Methanol	[21,94]
	Sodium oxalate	[52,70]
	Ammonium oxalate	[67,68,93]
	Potassium iodide	[23,95]
	Triethanolamine	[92]
H_2O_2	Fe(II)-EDTA	[83]
	Catalase	[95]
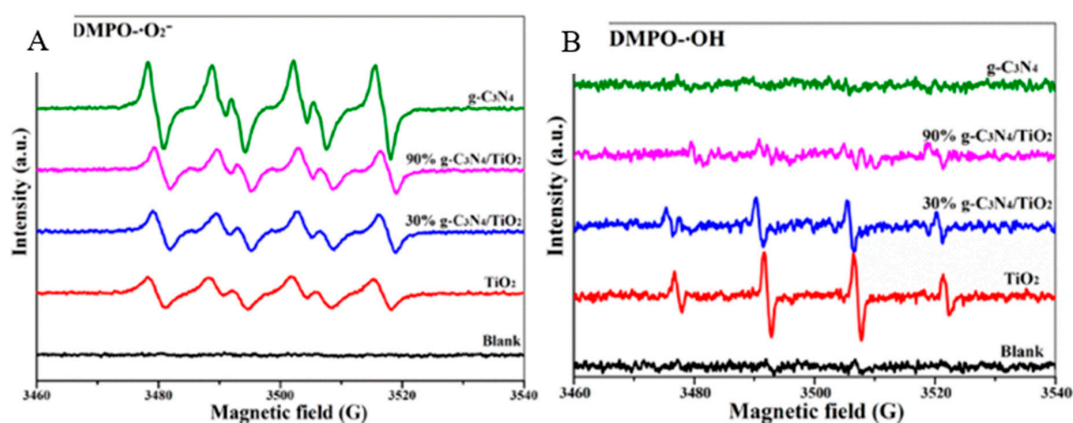
Figure 7. EPR results of (**A**) DMPO-$O_2^-\bullet$ and (**B**) DMPO-$\bullet$OH of pure TiO_2, 30 and 90% g-C_3N_4/TiO_2, and pure g-C_3N_4 under UV irradiation for 60 s. Reprinted from reference [74]. Copyright 2020 ACS.

Selective noble metal deposition. The electron/hole active sites are characteristic of each mechanism. The correct identification of the sites can provide very conclusive results. One simple approach to detect the charge active sites in the composite photocatalyst is selective metal deposition. Reduced metals will accumulate over electron active sites while oxidized metals will accumulate over hole active sites. After that, the deposited metals can be detected through transmission electron microscopy (TEM) imaging. This procedure was performed by Jiang et al. [21,72] to clarify the mechanism of g-C_3N_4/CdS, Fe_2O_3/g-C_3N_4, and TiO_2/CdS for hydrogen production by using Pt to detect electron active sites and PbO_2 to detect hole active sites, as shown in Figure 8.
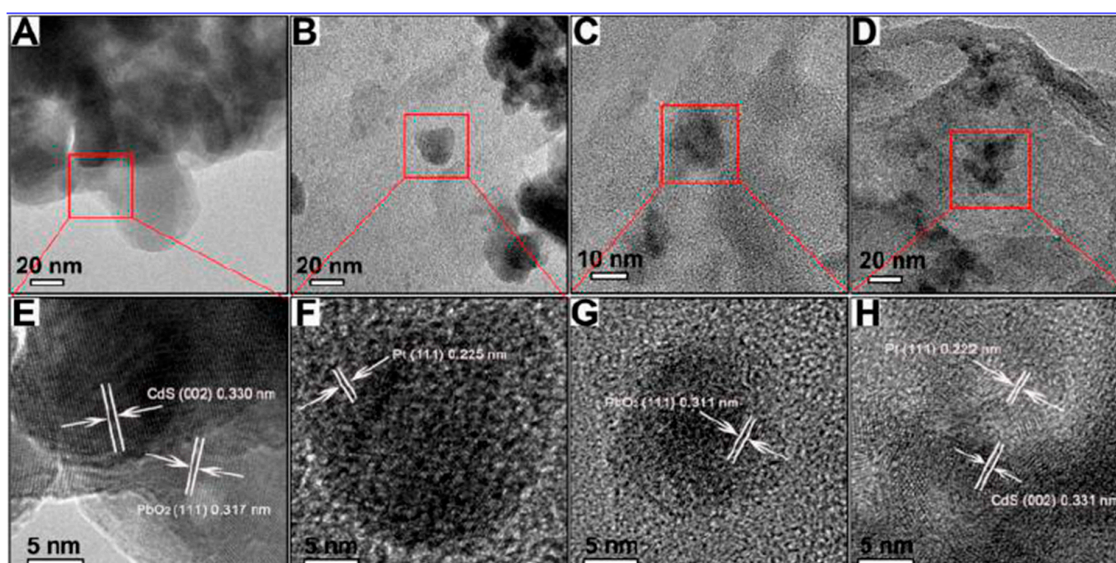
Figure 8. Charge transfer route of chemical deposition g-C$_3$N$_4$/CdS-10% and photodeposition g-C$_3$N$_4$/CdS-25. TEM images of g-C$_3$N$_4$/CdS-10% (**A,B,E,F**) and g-C$_3$N$_4$/CdS-25 (**C,D,G,H**) photodeposited with PbO$_2$ nanoparticles (**A,E,C,G**) and Pt (**B,F,D,H**) nanoparticles. (**E−H**) give the corresponding high-resolution TEM images, respectively. Reprinted from reference [68]. Copyright 2018 ACS.

Photocorrosion. Photocorrosion is a common phenomenon of metal sulfides and normally occurs due to the oxidation of surface sulfide ions (S^{2-}) by the photogenerated holes. Hence, this phenomenon can confirm the location of the holes in the composite. This self-oxidation process is irreversible and leads to the inhibition of the photocatalytic reaction [60]. Therefore, to study the stability of the photocatalysts, the most common tests are the transient photocurrent response and catalyst reuse. In the first case, current density is measured during several consecutive on–off irradiation cycles. In the second case, the photocatalytic reaction is performed for several cycles with the same catalyst. In both cases, a steady, reproducible response is a clear indicator of the catalyst stability. Figure 9A shows the photocurrent response of the ZnO/g-C$_3$N$_4$ composite with a remarkable decay of current density [75]. Figure 9B shows the performance of Cu$_2$O/g-C$_3$N$_4$ after several cycles [53]. The decrease in the photocatalytic activity points out the degradation of the catalyst. These kinds of stability tests are often found with CdS-based composites (TiO$_2$/CdS [52], CdS/g-C$_3$N$_4$ [72], and ZnO/CdS [98]).
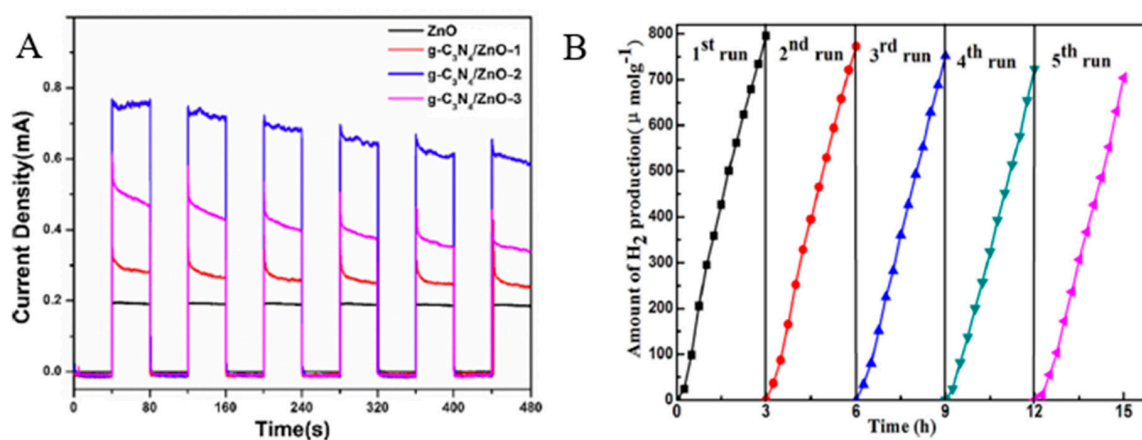
Figure 9. (**A**) Photocurrent response of ZnO/g-C$_3$N$_4$ composite. Reprinted from reference [71]. Copyright 2019 Elsevier. (**B**) H$_2$ evolution over Cu$_2$O/g-C$_3$N$_4$ reused sample. Reprinted from reference [53]. Copyright 2015 Elsevier.

In the next section, the use of the mentioned procedures in the identification of the charge transfer mechanism will be discussed.

3.1. Sensitization

The first photocatalytic works associated with the sensitization mechanism used a dye or a molecule that could be activated by visible light to start the electron transfer mechanism. The review of Ni et al. emphasized the photocatalytic hydrogen production of safranin–O–TiO$_2$ composites [10]. Hamilton et al. [17] highlighted the effectiveness of dyes like rhodamine B on extending TiO$_2$ response into the visible region for water disinfection.

In the case of a catalyst composed of two semiconductors, sensitization occurs when one of them is excited by the incident light and the second one acts as an electron sink. It is a well-known mechanism and therefore, several techniques have been developed for its identification [10].

The simplest procedure consists of the determination of the excitation of the semiconductor with a narrower band gap. For instance, both TiO$_2$ and SiC have a band gap of 3.2 eV with a corresponding absorption wavelength of 380 nm in the UV spectrum (Figure 1). On the other hand, graphitic carbon nitride (g-C$_3$N$_4$) has a band gap of 2.7 eV (Figure 1), which partially absorbs visible light [63]. Enhanced photocatalytic activity in the visible range is consistent proof of the interaction between the semiconductors. Bare TiO$_2$ (or SiC) under visible light illumination does not show photocatalytic activity. Moreover, the composite shows photogeneration of charges, observed in photocatalytic tests and photoluminescence measurements. Therefore, the second semiconductor triggers catalytic activity on TiO$_2$, which is strong supporting evidence of the sensitization mechanism. So, the first test should be excitation under different light sources such as UV light and visible light.

Hydrogen production enhancement through the sensitization mechanism has been widely reported and the main tests to verify this mechanism are UV/Vis illumination and photoluminescence spectra analysis. Isimjan et al. [74] prepared the composite TiO$_2$/g-C$_3$N$_4$ with promoted photo-charge separation under visible light compared to pure TiO$_2$ and g-C$_3$N$_4$, according to PL spectra analysis. H$_2$ production was 1.5-fold higher for the composite than for g-C$_3$N$_4$ alone. Yu et al. [42] successfully sensitized TiO$_2$ with carbon quantum dots (C), detecting photocatalytic hydrogen production under visible light illumination (Table 2). This is clear evidence of sensitization because TiO$_2$ is not active in the visible range. Wang et al. [45] synthesized SiC/g-C$_3$N$_4$ composites and proved the sensitization mechanism through hydrogen production under visible light (Table 2). Since SiC is not active under visible light, the electron source was attributed to g-C$_3$N$_4$. Zhang et al. [43] confirmed the sensitization of TiO$_2$ by C after detecting a broader photo-response and photocatalytic hydrogen production under visible light. Sargin et al. [44] also synthesized a TiO$_2$/C composite with enhanced catalytic activity under solar light illumination compared to bare TiO$_2$ with remarkable activity under visible light, thus confirming the sensitization. In Kim et al. [101], the recombination of charges in the TiO$_2$/CdS composite was lower than that in the bare components, according to the PL spectra. Moreover, hydrogen was obtained working under visible light, confirming the sensitization mechanism. The synthesized TiO$_2$/g-C$_3$N$_4$ composite also showed improved hydrogen production according to Tan et al. [102]. Sensitization was confirmed after band gap determination through the Kubelka–Munk equation. In the work of Luo et al., DFT was used to determine the band energies and interface charge transfer of SrTiO$_3$/g-C$_3$N$_4$, thus confirming the sensitization mechanism, because SrTiO$_3$ could only absorb the light with a wavelength lower than 390 nm [103].

Table 2. Charge transfer mechanism reported for different hybrid photocatalysts.

Mechanism	Catalyst	Objective	Sacrificial Agent	Light Source	Reference
Sensitization	TiO_2/C	H_2 production	Methanol	500 W Xe lamp ($\lambda > 450$ nm)	[42]
	TiO_2/C	H_2 production	Na_2S/Na_2SO_3	300 W Xe lamp (Visible region)	[43]
	TiO_2/C	H_2 production	TEOA	300 W Xe lamp ($\lambda > 420$ nm)	[44]
	SiC/g-C_3N_4	H_2 production	TEOA	300 W Xe lamp ($\lambda > 420$ nm)	[45]
	$Pd/TiO_2/g$-C_3N_4	H_2 production	TEOA	300 W Xe lamp ($\lambda > 420$ nm)	[74]
	TiO_2/g-C_3N_4/C	Dye degradation		500 W Xe lamp ($\lambda > 400$ nm)	[76]
	TiO_2/CdS	H_2 production	Na_2S/Na_2SO_3	300 W Xe lamp ($\lambda > 420$ nm)	[101]
	TiO_2/g-C_3N_4	H_2 production	TEOA	300 W Xe lamp ($\lambda > 420$ nm)	[102]
	$SrTiO_3/g$-C_3N_4	H_2 production	TEOA	300 W Xe lamp ($\lambda > 420$ nm)	[103]
	TiO_2/g-C_3N_4	Dye degradation		350 W Xe lamp ($\lambda > 420$ nm)	[104]
Direct Z-scheme	Fe_2O_3/g-C_3N_4 TiO_2/CdS	H_2 production	Na_2S/Na_2SO_3	300 W Xe lamp	[21]
	$WO_3/TiO_2/Pt$	H_2 production	Methanol	300 W Xe lamp	[25]
	g-$C_3N_4/BiVO_4$	H_2 production	$NaSO_3$	300 W Xe lamp ($\lambda > 420$ nm)	[27]
	TiO_2/CdS	Pollutant removal		150 W Xe lamp	[52]
	g-C_3N_4/Nb_2O_5	H_2 production	TEOA/Methanol	1000 W Xe lamp	[59]
	$CoTiO_3/g$-C_3N_4/Pt	H_2 production	Methanol	300 W Xe lamp ($\lambda > 420$ nm)	[69]
	CdS/g-C_3N_4	H_2 production	Na_2S/Na_2SO_3	300 W Xe lamp ($\lambda > 420$ nm)	[72]
	$Pt/TiO_2/g$-C_3N_4	H_2 production	TEOA	350 W Xe lamp	[77]
	TiO_2/g-C_3N_4	Pollutant removal		UV radiation	[78]
	TiO_2/g-C_3N_4	Pollutant removal		500 W Xenon lamp	[67]
	TiO_2/g-C_3N_4	Dye degradation		500 W Xe lamp	[68]
	TiO_2/g-C_3N_4	Water disinfection		300 W Xe lamp	[83]

Table 2. *Cont.*

Mechanism	Catalyst	Objective	Sacrificial Agent	Light Source	Reference
Direct Z-scheme	TiO_2/CdS	CO_2 reduction		300 W Xe lamp	[89]
	$CdS/CdWO_4$	H_2 production	Lactic acid	300 W Xe lamp ($\lambda > 420$ nm)	[93]
	$CoWO_4/CdS$	H_2 production	Na_2S/Na_2SO_3	300 W Xe lamp ($\lambda > 420$ nm)	[94]
	$TiO_2/g\text{-}C_3N_4$	Dye degradation		LED lamp 3 W ($\lambda = 365$ nm)	[96]
	TiO_2/CdS	H_2 production	Methanol	350 W Xe lamp	[97]
	ZnO/CdS	H_2 production	Na_2S/Na_2SO_3	350 W Xe lamp	[98]
	$BiVO_4/CdS$	H_2 production	Lactic acid	300 W Xe lamp ($\lambda > 420$ nm)	[105]
	WO_3/CdS	CO_2 reduction		300 W Xe lamp ($\lambda > 420$ nm)	[106]
	$\alpha Fe_2O_3/g\text{-}C_3N_4$	CO_2 reduction		Visible light	[107]
Type II heterojunction	$ZnO/g\text{-}C_3N_4$	Dye degradation		300 W Xe lamp	[23]
	TiO_2/CdS	Pollutant removal		150 W Xe lamp	[52]
	$Cu_2O/g\text{-}C_3N_4$	H_2 production	TEOA	300 W Xe lamp ($\lambda > 400$ nm)	[53]
	$g\text{-}C_3N_4/Nb_2O_5$	Pollutant removal		6x15 W visible light lamp	[70]
	$CdS/g\text{-}C_3N_4$	H_2 production	Na_2S/Na_2SO_3	300 W Xe lamp ($\lambda > 420$ nm)	[72]
	TiO_2/MoS_2	H_2 production	TEOA	300 W Xe lamp ($\lambda > 400$ nm)	[73]
	$ZnO/g\text{-}C_3N_4$	H_2 production	Na_2S/Na_2SO_3	300 W Xe lamp	[75]
	$B\text{-}TiO_2/g\text{-}C_3N_4$	H_2 production	Methanol	300 W Xe lamp ($\lambda > 400$ nm)	[66]
	$\beta Fe_2O_3/g\text{-}C_3N_4$	Dye degradation		300 W Xe lamp ($\lambda > 420$ nm)	[92]
	$Bi_2W_2O_9/g\text{-}C_3N_4$	Pollutant removal		35 W Xe lamp	[95]
	$TiO_2/g\text{-}C_3N_4$	H_2 production	Methanol	500 W Xe lamp	[108]
	NiS/CdS	H_2 production	Na_2S/Na_2SO_3	300 W Xe lamp ($\lambda > 420$ nm)	[109]
	TiO_2/NiO	H_2 production	Methanol	300 W Xe lamp ($\lambda > 400$ nm)	[110]
	TiO_2/NiO	H_2 production	Methanol	1.6 W Hg lamp ($320 < \lambda < 400$)	[111]

With respect to dye degradation, Hao et al. reported catalytic activity under visible light for the TiO_2/g-C_3N_4 composite [104]. Band gap alignment determination using empirical equations was also fundamental to determine the mechanism, concluding that carbon nitride had a sensitization effect over TiO_2.

3.2. Direct Z-Scheme

With regard to photocatalytic hydrogen production, some reports can be considered as water splitting when water molecules are the unique substrate for hydrogen production; however, in most cases, a sacrificial agent is added to enhance hydrogen production, as shown in Table 2. The scope of this review was aimed toward works where hydrogen production is carried out with sacrificial agents. Special attention needs to be focused on the sacrificial agent since it may influence the hydrogen production rate and catalyst activity. For example, the work of Idrees et al. explored the influence of two sacrificial agents, TEOA and methanol, over the photocatalytic performance of g-C_3N_4/Nb_2O_5, and even though the hydrogen production rate was highly influenced, it was not attributed to a different mechanism [59]. Tahir et al. also reported similar conclusions [34].

Concerning photocatalytic hydrogen production, it is worth mentioning the works of Jiang et al. [21,72], which reported that the Z-scheme mechanism was responsible for the activity of TiO_2/CdS, Fe_2O_3/g-C_3N_4, and CdS/g-C_3N_4 for photocatalytic hydrogen production. The authors performed radical trapping in order to determine the reactive oxygen species responsible for the degradation of rhodamine B. Benzoquinone, ammonium oxalate and isopropanol were used for trapping superoxide radicals ($\bullet O_2^-$), hydroxyl radicals ($\bullet OH$) and holes, respectively. All radicals were detected, but the interesting breakthrough was that only the CB of g-C_3N_4 had the redox potential to produce superoxide radicals ($E_{CB} = -1.09$ eV; $E(O_2/\bullet O_2^-) = -0.33$ eV vs. NHE) and, at the same time, only Fe_2O_3 had the redox potential to produce hydroxyl radicals ($E_{VB} = 2.41$ eV; $E(OH^-/\bullet OH) = 1.96$ eV). If the charge transfer mechanism followed the type II heterojunction, no superoxide or hydroxyl radicals would have been detected. However, according to the direct Z-scheme mechanism, the strong redox potential is retained and thus, the radicals can be generated. The same situation was observed while testing the performance of TiO_2/CdS and CdS/g-C_3N_4 photocatalysts for the same application [21]. In order to detect active sites, the authors performed the reduction of Pt to locate electrons and the oxidation of PbO_2 to locate holes. It was reported that reduction of Pt occurred exclusively over g-C_3N_4 and PbO_2 was only found over Fe_2O_3. In the case of TiO_2/CdS, PbO_2 appeared over the TiO_2 while Pt was reduced over CdS. The activity in both cases was explained through the formation of the direct Z-scheme mechanism because CdS and g-C_3N_4 acted as electron active sites, and TiO_2 and Fe_2O_3 acted as hole active sites, respectively [21]. In the case of the last semiconductor (CdS/g-C_3N_4), Pt was found over g-C_3N_4 with the highest conduction band and PbO_2 over CdS with the lowest valence band, confirming the direct Z-scheme.

In some cases, hydrogen production serves as interesting evidence of the existence of the direct Z-scheme. A semiconductor cannot perform redox reactions that are below the conduction band or above the valence band. In type II heterojunction, these boundaries are established by the lowest conduction band in SCII and the highest valence band in SCI (Figure 3C). On the other hand, the boundaries of direct Z-scheme semiconductors are established by the highest conduction band in SCI and the lowest valence band in SCII (Figure 3D). Thus, some reactions are feasible only for composites acting under the direct Z-scheme mechanism. For example, using the $CoTiO_3$/g-C_3N_4 composite for photocatalytic hydrogen generation, Ye et al. concluded that hydrogen production and radical generation were not possible if the type II heterojunction was the charge transfer mechanism because the accumulated electrons from the CB of $CoTiO_3$ cannot reduce O_2 to form $\bullet O_2^-$ as well as h^+ into H_2. Nevertheless, both hydrogen and superoxide radicals were found in the photocatalytic activity tests and radical trapping tests, respectively. Therefore, the authors concluded that g-C_3N_4 was the electron active site and the direct Z-scheme was the most suitable mechanism [69]. Photocatalytic hydrogen production was also used as experimental evidence by Gao et al. to determine the mechanism

of WO_3/TiO_2 since the calculated conduction band of WO_3 (0.5 eV) did not have a reduction potential high enough to produce hydrogen (0 eV) [25]. However, the authors observed hydrogen formation and related it to the synergistic effect between semiconductors as it was higher than the production of the bare components. Hydrogen production also supported the direct Z-scheme in the use of the $BiVO_4/CdS$ photocatalyst for photocatalytic hydrogen production synthesized by Zhou et al. [105] where the conduction band of $BiVO_4$ (0.1 eV) did not have the right potential to produce hydrogen. However, the conduction band of CdS (−0.85 eV) was suitable and, additionally, they proved the absence of holes in the CdS because photocorrosion was avoided. The activity of $g\text{-}C_3N_4/Nb_2O_5$ production was also attributed to the direct Z-scheme due to the significant increase in hydrogen production compared to individual components under simulated solar light illumination, reduced recombination rate, and staggered band positions, as reported by Idrees et al. [59]. Si et al. also reported enhanced hydrogen production using $g\text{-}C_3N_4/BiVO_4$ [27]. Hydroxyl radicals were detected using terephthalic acid as the scavenger. These radicals are hardly produced by graphitic carbon (E_{VB} = 1.53 eV; $E(OH^-/\bullet OH)$ = 2.4 eV vs. NHE), but the VB of $BiVO_4$ (E_{VB} = 3.05 eV) possessed enough oxidizing potential to generate $\bullet OH$. Nevertheless, the authors concluded that further tests like the trapping of other radical species and/or selective noble metal deposition should be conducted to give a conclusive result regarding the mechanism. The reported high stability of the ZnO/CdS composite, together with the detection of hydroxyl radicals and enhanced hydrogen production, served to support the direct Z-scheme mechanism by Wang et al. [98]. Jia et al. also detected hydroxyl radicals and the high stability of $CdS/CdWO_4$ and supported the direct Z-scheme mechanism [93]. Furthermore, they conducted Pt reduction experiments to determine electron active sites, and found that the metal was reduced over CdS and therefore the direct Z-scheme mechanism was confirmed. Meng et al. synthesized TiO_2/CdS and confirmed the direct Z-scheme mechanism because hydroxyl radicals were detected, which is only compatible with the direct Z-scheme, according to the XPS-determined band positions [97]. Transient photocurrent response confirmed the stability of the composite, proving that CdS does not act as a hole sink, so did not undergo photocorrosion. The same tests were performed by Cui et al. to corroborate the direct Z-scheme in the $CoWO_4/CdS$ composite [94]. High stability as well as enhanced degradation of pollutants and detected ROS inTiO_2/CdS reported by Zhang et al. evidenced that the charge transfer mechanism was the direct Z-scheme [52]. According to the conclusions gathered so far, photocorrosion in CdS-based composites can be explained by the type II heterojunction mechanism due to the location of holes on the CdS. Working with $TiO_2/g\text{-}C_3N_4$, Wang et al. observed improved photocatalytic hydrogen production as well as more efficient separation of electron/hole pairs determined by photoluminescence spectra compared to that of the bare components [77]. Furthermore, the detection of hydroxyl radicals, as in previous works, helped and supported the direct Z-scheme as the main mechanism responsible for the photocatalytic process.

Several works in the field of photocatalytic pollutant degradation have contributed to the discrimination of the charge transfer mechanism. When $TiO_2/g\text{-}C_3N_4$ composites were used for dye and antibiotic removal, the direct Z-scheme was confirmed after band gap determination and radical trapping since the presence of hydroxyl and superoxide radicals did not match the type II heterojunction charge transfer because the VB potential of CN (1.575 eV) was much lower than the required potential for $\bullet OH$ generation ($H_2O/\bullet OH$ = 2.4 eV). Moreover, electron-hole recombination decrease was confirmed through the PL spectra [67,78,96]. Liu et al. supported the direct Z-scheme mechanism in the application of $TiO_2/g\text{-}C_3N_4$ composites for photocatalytic water disinfection by radical species determination [83]. The most remarkable species detected were hydroxyl and superoxide radicals. Further evidence was provided such as enhanced photocatalytic activity of the composite compared to the bare components and reduction of electron-hole recombination, as demonstrated by the PL spectra. Working with the same photocatalyst, Huang et al. also reported that the direct Z-scheme was responsible for methyl orange (MO) degradation [68]. The authors concluded that the strong interaction and high separation rate of electron/hole pairs between TiO_2 and $g\text{-}C_3N_4$ enhanced

the photocatalytic degradation of the dye. The detected radicals ($\bullet OH$, $O_2^-\bullet$, and h^+) together with the band positions calculated through empirical equations pointed to the direct Z-scheme.

The direct Z-scheme mechanism has also been proposed as responsible for the photocatalytic activity for CO_2 reduction. When using TiO_2/CdS, the mechanism was supported after the detection of hydroxyl radicals and with the XPS-estimated band energies, as reported by Low et al. [89]. The main product of this photocatalytic process was methane. The work reported by Jin et al. confirmed the existence of the direct Z-scheme in the CdS/WO_3 composite by performing the photocatalytic reduction of CO_2 and detecting hydroxyl radicals [106]. Methane production was demonstrated because the only configuration able to produce methane was the direct Z-scheme, since the CB of CdS (-0.6 eV) had enough reduction potential to convert CO_2 to methane (-0.24 eV), but the CB of WO_3 did not (0.5 eV). On the other hand, the valence band with an oxidation potential high enough to produce hydroxyl radicals ($OH^-/\bullet OH = 2.4$ eV) was the VB of WO_3 (3.0 eV) as the VB of CdS (1.7 eV) was below the required potential to generate hydroxyl radicals. Moreover, low photocorrosion was additional proof of the absence of holes in the CdS part, which is susceptible to oxidation. The detection of superoxide and hydroxyl radicals in the Fe_2O_3/g-C_3N_4 composite reported by Jiang et al. proved the existence of the direct Z-scheme according to the band determination through XPS and enhanced methane production [107].

3.3. Type II Heterojunction

Most of the works that have proposed the type II mechanism do not provide as much evidence as works that support the direct Z-scheme hypothesis. It is common to find PL spectra to confirm the reduction of the recombination of charges and band alignment determination to support the mechanism, considering that charge transfer from high to low band energies is the thermodynamically favored path. In fact, this is the case for all the articles summarized in Table 2. Although all the characterization techniques proposed above are completely valid for both type II heterojunction and the direct Z-scheme, not all of them are performed at the same time. Nevertheless, the following references were selected for having conducted at least one of the proposed tests to clarify the mechanism.

Regarding hydrogen production, Chen et al. [66] reported that the addition of g-C_3N_4 widened the absorption to the visible light region, resulting in more efficient utilization of the solar spectrum according to the absorption spectrum and higher hydrogen production. Moreover, TiO_2/g-C_3N_4 boron doping favored the visible light absorption and increased electron trapping centers, which inhibited recombination and promoted electron transfer from the CB of carbon nitride to the CB of titanium dioxide. According to the authors, since the VB of TiO_2 (2.44 eV) was higher than the VB of carbon nitride (1.4 eV), holes migrated from TiO_2 to g-C_3N_4. Electrons followed the reverse path, from the CB of g-C_3N_4 (-1.3 eV) to the CB of TiO_2 (-0.46 eV), thus proving type II heterojunction. However, more defining evidences and further evaluations should be performed such as UV/Vis tests to determine sensitization and radical trapping or metal deposition to confirm electron/hole active sites. Enhanced H_2 production of TiO_2/g-C_3N_4 compared to that of the pure components was also described by Raziq et al. [108]. They also detected a decrease in photoluminescence compared to that of the bare components and therefore a reduction in photoinduced charge transfer recombination. All these data as well as the band alignment were used to conclude that the type II heterojunction occurred, although it could also match the direct Z-scheme. Further tests like radical trapping could shed light to clarify the mechanism. Jiang et al. determined the CdS/g-C_3N_4 type II heterojunction mechanism by performing selective noble metal deposition and radical trapping, the same procedure as that detailed previously for the direct Z-scheme CdS/g-C_3N_4 composite [72]. However, in this case, Pt reduction happened over CdS while PbO_2 oxidation happened over g-C_3N_4, confirming that CdS acted as the electron sink and carbon nitride as the hole sink. Hence, electrons migrated from the CB of g-C_3N_4 (-1.28 eV) to the CB of CdS (-0.58 eV) and holes moved from the VB of CdS (1.97 eV) to the VB of g-C_3N_4 (1.59 eV). Liu et al. [53] concluded that electrons could easily transfer from the Cu_2O CB to the g-C_3N_4 CB due to band alignment. Furthermore, enhanced hydrogen production was also reported, concluding that type

II heterojunction was the charge transfer mechanism. Zhang et al. selectively deposited CdS on the {001} facet of poor photostability and weakened redox abilities compared to the direct Z-scheme composite in which CdS was selectively deposited on the {101} facet of TiO_2 [52]. With further evidence such as band position determination, the work concluded that the existence of type II heterojunction. Liu et al. calculated band positions and led to the conclusion that photogenerated electrons could easily transfer from CB of g-C_3N_4 to CB of ZnO due to the more negative CB position of CdS and the photogenerated holes could easily move from the VB of ZnO to the VB of g-C_3N_4 due to the more positive VB position of ZnO [68]. This was further supported by the stability of the composite since the type II heterojunction mechanism could prevent ZnO photocorrosion. NiS/CdS heterostructure synthetized by Zhang et al. for photocatalytic water splitting showed excellent visible light hydrogen production and high stability. Band positions suggested that NiS–CdS could form stable type II heterojunctions where NiS would act as the hole sink, preventing CdS from photocorrosion [109]. Wang et al. concluded that type II heterojunction was the transfer mechanism of the TiO_2/NiO composite based on the band position and band alignment added to improve the photocatalytic production of H_2 and degradation of rhodamine B [110]. Hu et al. reported that the selectively deposited MoS_2/TiO_2 composite exhibited high photocatalytic H2 evolution activity with a rate as high as 2.16 mmol h^{-1} g^{-1} for the sample with 15 wt% MoS_2 loading, which was 32-fold and 3-fold more than the pure TiO_2 and MoS_2/TiO_2 composites, respectively [73]. The proposed mechanism was attributed to the different facets of TiO_2 that have different band positions and, therefore, charge transfer could occur. Since electrons moved from the 001 surface on the CB facet to MoS_2, this acted as an electron sink and holes accumulated on that mentioned surface. Uddin et al. also reported enhanced hydrogen production and, in combination with band gap determination through XPS, concluded that that it was type II heterojunction in the case of TiO_2/NiO composite [111].

In order to test the photocatalytic behavior of the composites, some works have conducted the photocatalytic degradation of organic compounds. Wu et al. proposed t6he type II heterojunction charge transfer mechanism because the synthesized ZnO/g-C_3N_4 composite showed superior stability and enhanced photocatalytic degradation of rhodamine B under simulated solar sunlight, exciting both components of the catalyst [23]. Moreover, no hydroxyl radicals were detected during radical test trapping, proving that hole active sites remained in g-C_3N_4. The Fe_2O_3/g-C_3N_4 composite synthetized by Christoforidis et al. also followed the type II heterojunction mechanism in the removal of rhodamine B and methyl orange after performing band gap determination and the radical trapping test under visible light, exciting both Fe_2O_3 and g-C_3N_4 [92]. The g-C_3N_4/Nb_2O_5 heterostructures of da Silva et al. [70] exhibited higher photocatalytic activity toward the oxidation of rhodamine B (RhB) and amiloride (AML) compared to bare g-C_3N_4 and Nb_2O_5. Band position confirmed that electrons could easily go from the CB of g-C_3N_4 (−1.23 eV) to the CB of Nb_2O_5 (−0.8 eV). The longer lifetime of the photogenerated charges also supported the type II heterojunction mechanism. $Bi_2W_2O_9$/g-C_3N_4 also demonstrated a higher degradation of tetracycline than the bare components, according to the report by Obregon et al. [95]. Radical trapping tests confirmed the existence of the type II heterojunction.

Some of the proposed evidences are common to all the mechanisms and provide general information about the redox potential and optical properties of the photocatalyst. Even though the rest of the techniques used to identify the direct Z-scheme and type II heterojunction are the same, the results are opposite. For example, radical generation is often characteristic of direct Z-scheme, whilst photocorrosion is usually indicative of type II heterojunction. In the case of metal deposition, each mechanism has characteristic charge active sites and the results are exclusive of a certain mechanism.

4. Conclusions and Further Perspectives

The quest for ideal photocatalysts relies on the development of semiconductor materials with enhanced capacity to absorb light in the visible part of the solar spectrum and with high stability to be used for long operation times. In this search, semiconductor–semiconductor heterojunctions stand out

and have given rise to a good number of materials with promising prospects to contribute to worldwide environmental and energy issues. Since the first cost-effective and widely used metal oxides such as TiO_2 or ZnO, the design of photocatalysts has evolved considerably. So far, several composites such as TiO_2/g-C_3N_4, TiO_2/CdS, g-C_3N_4/Nb_2O_5, ZnO/CdS, or TiO_2/NiO have shown noteworthy results in photocatalytic hydrogen production and other photocatalysts like WO_3/CdS or $\alpha Fe_2O_3/g$-C_3N_4 have also shown outstanding performance regarding CO_2 reduction or pollutant degradation, paving the way toward efficiently harnessing visible light. The progress achieved in the synthesis of new photocatalysts demands in-depth knowledge of the role that every component plays in the performance of the final composite.

This article provides a thorough analysis of already published literature in the photocatalytic generation of hydrogen focused on identifying the charge transfer mechanism that ultimately determines the photocatalyst performance. There is a variety of possible mechanisms for every semiconductor–semiconductor heterostructure: (i) the sensitization mechanism, in which only one of the semiconductors is excited by the incident light and the non-excited semiconductor acts as electron sink; (ii) the direct Z-scheme, where the VB of SCI and the CB of SCII with the highest redox potential are preserved and electrons of the CB of SCI recombine with holes of the VB of SCII; and (iii) the type II heterojunction, where charges move from high energy bands to low energy bands, holes go from the VB of SCI to the VB of SCII, and electrons go from the CB of SCI to the CB of SCII.

To identify the proper mechanism, some general guidelines can be proposed. When the heterostructure shows different photocatalytic behavior under UV or visible light and interaction between semiconductors is confirmed, the charge transfer mechanism is sensitization. Nevertheless, this mechanism is compatible with the direct Z-scheme and type II heterojunction, because when both semiconductors are excited, the charge transfer may vary. Composites acting with the direct Z-scheme mechanism report enhanced photocatalytic performance and strong redox potential with good charge separation efficiency alongside additional characteristics such as the generation of radical oxidizing species; among them, the most common are superoxide and hydroxyl radicals. In the type II heterojunction mechanism, good efficiency in charge separation and enhanced production compared to that of the bare components have also been determined, but several drawbacks such as weakened redox potential compared to the direct Z-scheme and photocorrosion have been associated with this mechanism.

This article presents a fair number of techniques that provide experimental evidence supporting charge transfer mechanisms. Although great progress has been reported in the identification of the charge transfer mechanism, most of the references conclude the need for further evidence to allocate the charge transfer mechanism due to the inconclusive results observed in some cases. Band alignment and band gap determination, measured through XPS or diffuse reflectance, provide information useful for all mechanisms. The use of PL spectra is widespread, and has been proved to be effective at confirming the interaction between both semiconductors in a composite and the reduction of charge recombination. However, photoluminescence spectra measurement is defining evidence by itself, because the reduction of the recombination of the composites compared to bare components is shared by all the above-mentioned mechanisms. UV/Vis illumination has proven to be effective in the determination of the sensitization mechanism. Selective metal deposition is well defining evidence that clearly locates electrons and holes within the catalyst, but it is still not widely applied. Stability tests like transient photocurrent response and catalyst reuse are common in evaluating if the photocorrosion phenomenon deteriorates the catalytic material. Additionally, the stability test has been proven to be an effective method to determine hole active sites in composites that are likely to suffer from photocorrosion, especially in type II heterojunction. In this charge transfer mechanism, the performance decay is remarkable because of the accumulation of holes in the corrosion sensitive semiconductor within the composite. Regarding photocatalytic activity testing, dye degradation is not recommended since the existence of the dye sensitization effect over the catalyst remains unclear and may influence the photocatalytic performance.

Table 3 presents the experimental techniques and outcomes that have been applied to support the charge transfer mechanisms. As shown in the table, PL spectroscopy is essential to determine the reduction of charge recombination and interaction between semiconductors as supported by almost all of the reported articles in this review, regardless of the mechanism. Band gap and band alignment determination is also regarded as an essential test. Nevertheless, it is highly used to support type II heterojunction, probably because it proves that electrons follow the thermodynamically favored path from a higher energy band to a lower energy band. Regarding the direct Z-scheme, radical generation stands out as the most employed evidence, definitely relating radical species generation to the direct Z-scheme. Finally, it is necessary to highlight the need to carry out different tests for a given composite to support and conclude the most likely mechanism.

Table 3. Summary of the mechanisms and related characterization methods.

Supporting Information			
Mechanism	**Evidence**	**Characterization Technique**	**References**
Common evidences to all charge transfer mechanisms	Reduction of charge recombination	Photoluminescence spectra	[23,27,42–45,49,52,53, 58,63–71,74,93,95,96, 101–104,106,108–110]
	Band gap and band alignment	Diffuse reflectance	[23,27,42–45,49,52,53, 58,63–71,74,93,95,96, 101–104,106,108–110]
		XPS	
		Others (UPS, DFT)	
Sensitization	Electron transfer	UV/Vis illumination	[42–45,74,76,101–104]
Direct Z-scheme	Radical generation	Radical trapping	[20,53,62,63,65,66,85, 89,90,92,93,103]
		EPR	[69,78,107]
	Electron/hole active sites	Selective noble metal deposition	[21,72,93]
		Performance of different reactions	[69,105]
	Photocorrosion	Catalyst reuse	[72,93,97]
		Transient photocurrent response	[52,94,97,98,106]
Type II heterojunction	Radical generation	Radical trapping	[23,27,52,70,92,95]
	Electron/hole active sites	Selective noble metal deposition	[72]
		Performance of different reactions	[108]
	Photocorrosion	Catalyst reuse	[53,75]
		Transient photocurrent response	[52,75,109]

In summary, and according to reported information, the most stable catalysts with the best performance and higher use of the visible light spectrum regarding hydrogen production were those that followed the direct Z-scheme compared to the same composites that developed the type II heterojunction.

As further steps concerning photocatalytic hydrogen production, it is worth considering that the use of sacrificial agents may influence the results, since the redox potential of these agents vary from one to another and, depending on the band positioning of the composite, the photocatalytic hydrogen

reaction may be hindered when changing the sacrificial agent. Therefore, the role of sacrificial agents in mechanism determination should be explored.

Regarding future trends, this report further states the remarkable role of g-C_3N_4, as a stable, inexpensive semiconductor, with consistent hydrogen production and versatile photocatalytic applications. It is one of the most prominent materials within all the photocatalysts and composites reported because it is excited by visible light, easy to obtain, inexpensive, and has a graphene-like structure that can provide a high specific area. QD-based photocatalysts show noteworthy activity in hydrogen production because band energies can be controlled by the size change of quantum dots, providing new possibilities to control the response and light absorption properties, among others. Some of the disclosed articles like that by Tahir et al. [34] point to new charge transfer mechanisms such as the S-type heterojunction, which has a resemblance to the direct Z-scheme but an internal electric field is formed. Therefore, the already detailed characterization techniques need to be further exploited to determine the existence of this mechanism in addition to discriminating whether semiconductors are n-type or not.

To sum up, Figure 10 shows a decision-making diagram in order to help in the discrimination of the charge transfer mechanism responsible for the photocatalyst performance.
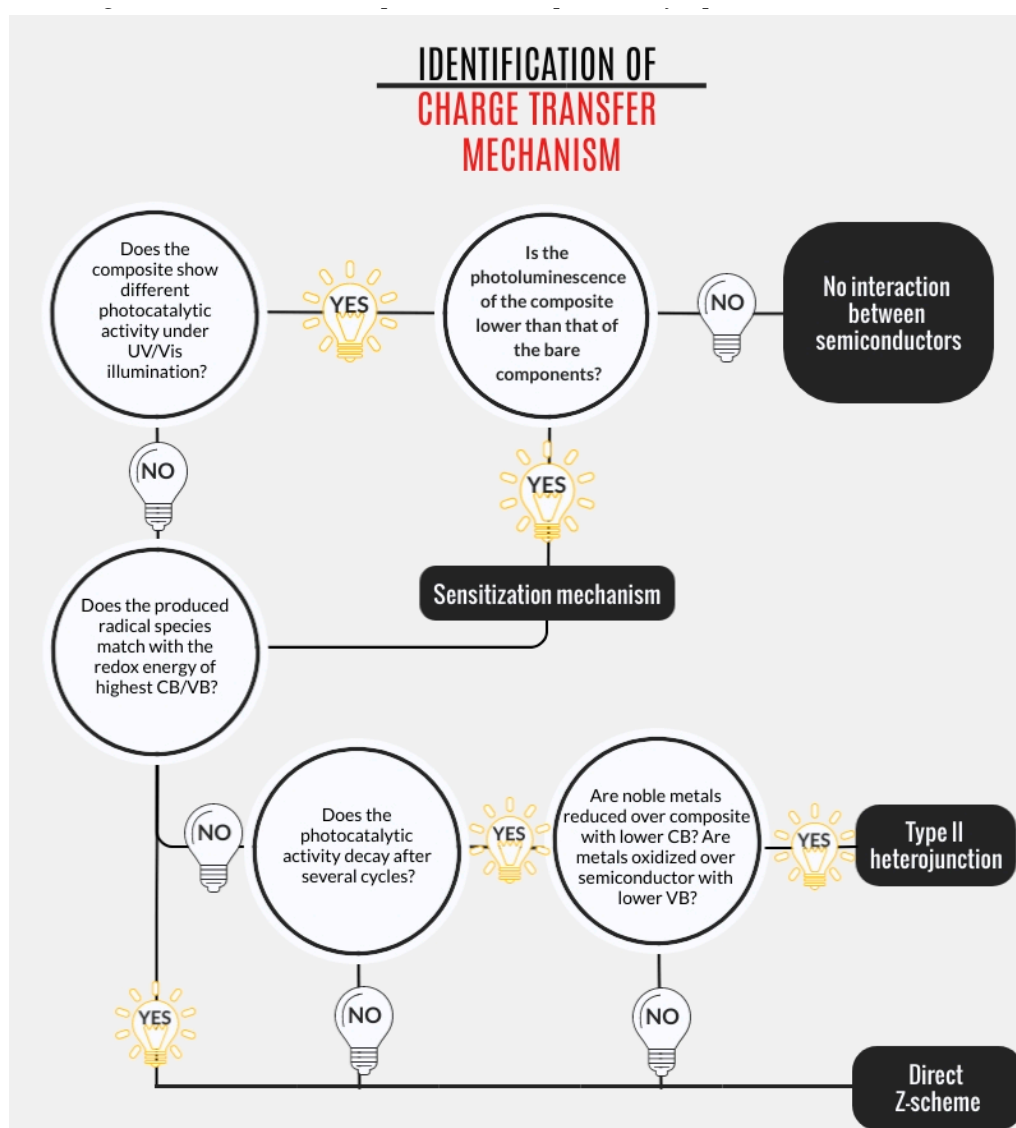

Figure 10. Decision-making diagram for charge transfer mechanism discrimination.

The diagram shows the route to discriminate between the charge transfer mechanisms by using experimental information. For instance, the composite may show different behavior under UV or visible light illumination, but if the photoluminescence of the composite is similar to the photoluminescence of the bare components, it means that there is no synergistic effect between the semiconductors and therefore, the effect is the same as if the semiconductors were used individually. However, if the PL spectra reflect a change, it confirms the existence of that sensitization mechanism. Moreover, this behavior is fully compatible with the other two mechanisms, therefore further evidence such as photocorrosion and metal deposition will help to either confirm or discard the type II heterojunction or direct Z-scheme.

The reviewed literature clearly states the need to determine the charge transfer mechanism and directly relate it to the photocatalytic performance. This work provides the essential information and a wide variety of experimental techniques to retrieve them in order to help in the decision-making process to obtain harmonized, homogeneous results to establish a consensus about the mechanism of charge transfer in the photocatalytic generation of hydrogen.

Conflicts of Interest: The authors declare no conflicts of interest.

References

1. Schneider, J.; Kandiel, T.A.; Bahnemann, D. Solar photocatalytic hydrogen production: Current status and future challenges. In *Nanostructure Science and Technology*; Viswanathan, B., Subramanian, V. (Ravi), Lee, J.S., Eds.; Springer: New York, NY, USA, 2014; Volume 174, pp. 41–74.
2. Schneider, J.; Matsuoka, M.; Takeuchi, M.; Zhang, J.; Horiuchi, Y.; Anpo, M.; Bahnemann, D.W. Understanding TiO_2 Photocatalysis: Mechanisms and materials. *Chem. Rev.* **2014**, *114*, 9919–9986. [CrossRef] [PubMed]
3. Pellegrino, F.; Sordello, F.; Minella, M.; Minero, C.; Maurino, V. The role of surface texture on the photocatalytic H_2 production on TiO_2. *Catalysts* **2019**, *9*, 32. [CrossRef]
4. Corredor, J.; Rivero, M.J.; Rangel, C.M.; Gloaguen, F.; Ortiz, I. Comprehensive review and future perspectives on the photocatalytic hydrogen production. *J. Chem. Technol. Biotechnol.* **2019**, *94*, 3049–3063. [CrossRef]
5. Michaelides, E.E. (Stathis) (Ed.) *Energy Storage BT—Alternative Energy Sources*; Springer: Berlin/Heidelberg, Germany, 2012; pp. 343–381, ISBN 978-3-642-20951-2.
6. Wang, M.; Shen, S.; Li, L.; Tang, Z.; Yang, J. Effects of sacrificial reagents on photocatalytic hydrogen evolution over different photocatalysts. *J. Mater. Sci.* **2017**, *52*, 5155–5164. [CrossRef]
7. Etacheri, V.; Di Valentin, C.; Schneider, J.; Bahnemann, D.W.; Pillai, S.C. Visible-light activation of TiO_2 photocatalysts: Advances in theory and experiments. *J. Photochem. Photobiol. C: Photochem. Rev.* **2015**, *25*, 1–29. [CrossRef]
8. Jafari, T.; Moharreri, E.; Amin, A.S.; Miao, R.; Song, W.; Suib, S.L. Photocatalytic water splitting—The untamed dream: A review of recent advances. *Molecules* **2016**, *21*, 900. [CrossRef]
9. Wang, Q.; Domen, K. Particulate photocatalysts for light-driven water splitting: Mechanisms, challenges, and design strategies. *Chem. Rev.* **2019**, *120*, 919–985. [CrossRef]
10. Ni, M.; Leung, M.K.H.; Leung, D.Y.; Sumathy, K. A review and recent developments in photocatalytic water-splitting using TiO_2 for hydrogen production. *Renew. Sustain. Energy Rev.* **2007**, *11*, 401–425. [CrossRef]
11. Fujishima, A.; Honda, K. Electrochemical photolysis of water at a semiconductor electrode. *Nature* **1972**, *238*, 37–38. [CrossRef]
12. Kim, J.H.; Kwon, G.; Lim, H.; Zhu, C.; You, H.; Kim, Y.T. Effects of transition metal doping in Pt/M-TiO_2 (M = V, Cr, and Nb) on oxygen reduction reaction activity. *J. Power Sources* **2016**, *320*, 188–195. [CrossRef]
13. Hernandez, J.V.; Coste, S.; Murillo, A.G.; Romo, F.D.J.C.; Kassiba, A. Effects of metal doping (Cu, Ag, Eu) on the electronic and optical behavior of nanostructured TiO_2. *J. Alloy. Compd.* **2017**, *710*, 355–363. [CrossRef]
14. Ray, C.; Pal, T. Recent advances of metal–metal oxide nanocomposites and their tailored nanostructures in numerous catalytic applications. *J. Mater. Chem. A* **2017**, *5*, 9465–9487. [CrossRef]

15. Liu, L.; Wu, X.; Wang, L.; Xu, X.; Gan, L.; Si, Z.; Li, J.; Zhang, Q.; Liu, Y.; Zhao, Y.; et al. Atomic palladium on graphitic carbon nitride as a hydrogen evolution catalyst under visible light irradiation. *Commun. Chem.* **2019**, *2*, 2–9. [CrossRef]

16. Ribao, P.; Esteves, M.A.; Fernandes, V.R.; Rivero, M.J.; Rangel, C.; Ortiz, I. Challenges arising from the use of TiO₂/rGO/Pt photocatalysts to produce hydrogen from crude glycerol compared to synthetic glycerol. *Int. J. Hydrog. Energy* **2019**, *44*, 28494–28506. [CrossRef]

17. Pelaez, M.; Nolan, N.T.; Pillai, S.C.; Seery, M.K.; Falaras, P.; Kontos, A.G.; Dunlop, P.; Hamilton, J.; Byrne, J.A.; O'Shea, K.; et al. A review on the visible light active titanium dioxide photocatalysts for environmental applications. *Appl. Catal. B Environ.* **2012**, *125*, 331–349. [CrossRef]

18. Zhang, X.; Peng, T.; Song, S. Recent advances in dye-sensitized semiconductor systems for photocatalytic hydrogen production. *J. Mater. Chem. A* **2016**, *4*, 2365–2402. [CrossRef]

19. Chowdhury, P.; Malekshoar, G.; Ray, A.K.; Chowdhury, P. Dye-sensitized photocatalytic water splitting and sacrificial hydrogen generation: Current status and future prospects. *Inorganics* **2017**, *5*, 34. [CrossRef]

20. Wu, H.L.; Li, X.B.; Tung, C.H.; Wu, L.Z. Recent advances in sensitized photocathodes: From molecular dyes to semiconducting quantum dots. *Adv. Sci.* **2018**, *5*, 1700684. [CrossRef]

21. Jiang, W.; Qu, D.; An, L.; Gao, X.; Wen, Y.; Wang, X.; Sun, Z. Deliberate construction of direct Z-scheme photocatalysts through photodeposition. *J. Mater. Chem. A* **2019**, *7*, 18348–18356. [CrossRef]

22. Wang, J.; Wang, Z.; Qu, P.; Xu, Q.; Zheng, J.; Jia, S.; Chen, J.; Zhu, Z. A 2D/1D TiO₂ nanosheet/CdS nanorods heterostructure with enhanced photocatalytic water splitting performance for H2 evolution. *Int. J. Hydrog. Energy* **2018**, *43*, 7388–7396. [CrossRef]

23. Wu, S.; Zhao, H.J.; Li, C.F.; Liu, J.; Dong, W.; Zhao, H.; Wang, C.; Liu, Y.; Hu, Z.Y.; Chen, L.; et al. Type II heterojunction in hierarchically porous zinc oxide/graphitic carbon nitride microspheres promoting photocatalytic activity. *J. Colloid Interface Sci.* **2019**, *538*, 99–107. [CrossRef] [PubMed]

24. Dominguez, S.; Huebra, M.; Han, C.; Campo, P.; Nadagouda, M.; Rivero, M.J.; Ortiz, I.; Dionysiou, D.D. Magnetically recoverable TiO₂-WO₃ photocatalyst to oxidize bisphenol A from model wastewater under simulated solar light. *Environ. Sci. Pollut. Res.* **2016**, *24*, 12589–12598. [CrossRef] [PubMed]

25. Gao, H.; Zhang, P.; Hu, J.; Pan, J.; Fan, J.; Shao, G. One-dimensional Z-scheme TiO₂/WO₃/Pt heterostructures for enhanced hydrogen generation. *Appl. Surf. Sci.* **2017**, *391*, 211–217. [CrossRef]

26. Prabhu, S.; Cindrella, L.; Kwon, O.J.; Mohanraju, K. Photoelectrochemical, photocatalytic and photochromic performance of rGO-TiO₂-WO₃ composites. *Mater. Chem. Phys.* **2019**, *224*, 217–228. [CrossRef]

27. Si, Y.H.; Chen, W.M.; Shang, S.K.; Xia, Y.; Zeng, X.-R.; Zhou, J.; Li, Y.Y. g-C₃N₄/Pt/BiVO₄ nanocomposites for highly efficient visible-light photocatalytic removal of contaminants and hydrogen generation. *Nanotechnology* **2020**, *31*, 125706. [CrossRef]

28. Wang, H.; Zhang, L.; Chen, Z.; Hu, J.; Li, S.; Wang, Z.; Liu, J.; Wang, X. Semiconductor heterojunction photocatalysts: Design, construction, and photocatalytic performances. *Chem. Soc. Rev.* **2014**, *43*, 5234–5244. [CrossRef]

29. Moniz, S.J.A.; Shevlin, S.A.; Martin, D.J.; Guo, Z.; Tang, J. Visible-light driven heterojunction photocatalysts for water splitting—A critical review. *Energy Environ. Sci.* **2015**, *8*, 731–759. [CrossRef]

30. Yang, Q.; Dong, L.; Su, R.; Hu, B.; Wang, Z.; Jin, Y.; Wang, Y.; Besenbacher, F.; Dong, M. Nanostructured heterogeneous photo-catalysts for hydrogen production and water splitting: A comprehensive insight. *Appl. Mater. Today* **2019**, *17*, 159–182. [CrossRef]

31. Fajrina, N.; Tahir, M. A critical review in strategies to improve photocatalytic water splitting towards hydrogen production. *Int. J. Hydrog. Energy* **2019**, *44*, 540–577. [CrossRef]

32. Kandi, D.; Martha, S.; Parida, K. Quantum dots as enhancer in photocatalytic hydrogen evolution: A review. *Int. J. Hydrog. Energy* **2017**, *42*, 9467–9481. [CrossRef]

33. Rao, V.; Reddy, N.; Kumari, M.; Cheralathan, K.; Ravi, P.; Sathish, M.; Neppolian, B.; Reddy, K.R.; Shetti, N.P.; Prathap, P.; et al. Sustainable hydrogen production for the greener environment by quantum dots-based efficient photocatalysts: A review. *J. Environ. Manag.* **2019**, *248*, 109246. [CrossRef] [PubMed]

34. Tahir, M.; Tasleem, S.; Tahir, B. Recent development in band engineering of binary semiconductor materials for solar driven photocatalytic hydrogen production. *Int. J. Hydrog. Energy* **2020**, *45*, 15985–16038. [CrossRef]

35. Zhao, Z.; Sun, Y.; Dong, F. Graphitic carbon nitride based nanocomposites: A review. *Nanoscale* **2015**, *7*, 15–37. [CrossRef] [PubMed]

36. Ong, W.J.; Tan, L.L.; Ng, Y.H.; Yong, S.T.; Chai, S.P. Graphitic carbon nitride (g-C_3N_4)-based photocatalysts for artificial photosynthesis and environmental remediation: Are we a step closer to achieving sustainability? *Chem. Rev.* **2016**, *116*, 7159–7329. [CrossRef]

37. Zheng, L.; Teng, F.; Ye, X.; Zheng, H.; Fang, X. Photo/electrochemical applications of metal Sulfide/TiO_2 heterostructures. *Adv. Energy Mater.* **2019**, *10*, 1902355. [CrossRef]

38. Li, X.; Shen, R.; Ma, S.; Chen, X.; Xie, J. Graphene-based heterojunction photocatalysts. *Appl. Surf. Sci.* **2018**, *430*, 53–107. [CrossRef]

39. Wen, J.; Xie, J.; Chen, X.; Li, X. A review on g-C_3N_4 -based photocatalysts. *Appl. Surf. Sci.* **2017**, *391*, 72–123. [CrossRef]

40. Fu, J.; Yu, J.; Jiang, C.; Cheng, B. g-C_3N_4-Based heterostructured photocatalysts. *Adv. Energy Mater.* **2017**, *8*, 1701503. [CrossRef]

41. Borgarello, E.; Kiwi, J.; Graetzel, M.; Pelizzetti, E.; Visca, M. Visible light induced water cleavage in colloidal solutions of chromium-doped titanium dioxide particles. *J. Am. Chem. Soc.* **1982**, *104*, 2996–3002. [CrossRef]

42. Yu, H.; Zhao, Y.; Zhou, C.; Shang, L.; Peng, Y.; Cao, Y.; Wu, L.Z.; Tung, C.H.; Zhang, T. Carbon quantum dots/TiO_2 composites for efficient photocatalytic hydrogen evolution. *J. Mater. Chem. A* **2014**, *2*, 3344–3351. [CrossRef]

43. Zhang, X.; Wang, F.; Huang, H.; Li, H.; Han, X.; Liu, Y.; Kang, Z. Carbon quantum dot sensitized TiO_2 nanotube arrays for photoelectrochemical hydrogen generation under visible light. *Nanoscale* **2013**, *5*, 2274–2278. [CrossRef] [PubMed]

44. Sargin, I.; Yanalak, G.; Arslan, G.; Patir, I.H. Green synthesized carbon quantum dots as TiO_2 sensitizers for photocatalytic hydrogen evolution. *Int. J. Hydrog. Energy* **2019**, *44*, 21781–21789. [CrossRef]

45. Wang, B.; Zhang, J.; Huang, F. Enhanced visible light photocatalytic H_2 evolution of metal-free g-C_3N_4 /SiC heterostructured photocatalysts. *Appl. Surf. Sci.* **2017**, *391*, 449–456. [CrossRef]

46. Xu, Q.; Zhang, L.; Yu, J.; Wageh, S.; Al-Ghamdi, A.A.; Jaroniec, M. Direct Z-scheme photocatalysts: Principles, synthesis, and applications. *Mater. Today* **2018**, *21*, 1042–1063. [CrossRef]

47. Li, H.; Zhou, Y.; Tu, W.; Ye, J.; Zou, Z. State-of-the-art progress in diverse heterostructured photocatalysts toward promoting photocatalytic performance. *Adv. Funct. Mater.* **2015**, *25*, 998–1013. [CrossRef]

48. Low, J.; Jiang, C.; Cheng, B.; Wageh, S.; Al-Ghamdi, A.A.; Yu, J. A review of direct Z-scheme photocatalysts. *Small Methods* **2017**, *1*, 1700080. [CrossRef]

49. People, R.; Bean, J.C. Band alignments of coherently strained GexSi1−x/Si heterostructures on ⟨001⟩ GeySi1−y substrates. *Appl. Phys. Lett.* **1986**, *48*, 538–540. [CrossRef]

50. Baker, D.R.; Kamat, P. Photosensitization of TiO_2Nanostructures with CdS quantum dots: Particulate versus tubular support architectures. *Adv. Funct. Mater.* **2009**, *19*, 805–811. [CrossRef]

51. Sun, W.T.; Yu, Y.; Pan, H.Y.; Gao, X.F.; Chen, Q.; Peng, L.M. CdS quantum dots sensitized TiO_2 nanotube-array photoelectrodes. *J. Am. Chem. Soc.* **2008**, *130*, 1124–1125. [CrossRef]

52. Zhang, J.; Zhou, D.; Dong, S.; Ren, N. Respective construction of Type-II and direct Z-scheme heterostructure by selectively depositing CdS on {001} and {101} facets of TiO_2 nanosheet with CDots modification: A comprehensive comparison. *J. Hazard. Mater.* **2019**, *366*, 311–320. [CrossRef]

53. Liu, L.; Qi, Y.; Hu, J.; Liang, Y.H.; Cui, W. Efficient visible-light photocatalytic hydrogen evolution and enhanced photostability of core@shell Cu_2O@g-C_3N_4 octahedra. *Appl. Surf. Sci.* **2015**, *351*, 1146–1154. [CrossRef]

54. Xia, X.; Song, M.; Wang, H.; Zhang, X.; Sui, N.; Zhang, Q.; Colvin, V.L.; Yu, W.W. Latest progress in constructing solid-state Z scheme photocatalysts for water splitting. *Nanoscale* **2019**, *11*, 11071–11082. [CrossRef] [PubMed]

55. Bard, A.J. Photoelectrochemistry and heterogeneous photo-catalysis at semiconductors. *J. Photochem.* **1979**, *10*, 59–75. [CrossRef]

56. Sayama, K.; Mukasa, K.; Abe, R.; Abe, Y.; Arakawa, H. A new photocatalytic water splitting system under visible light irradiation mimicking a Z-scheme mechanism in photosynthesis. *J. Photochem. Photobiol. A Chem.* **2002**, *148*, 71–77. [CrossRef]

57. Tada, H.; Mitsui, T.; Kiyonaga, T.; Akita, T.; Tanaka, K. All-solid-state Z-scheme in CdS–Au–TiO_2 three-component nanojunction system. *Nat. Mater.* **2006**, *5*, 782–786. [CrossRef]

58. Yu, J.; Wang, S.; Low, J.; Xiao, W. Enhanced photocatalytic performance of direct Z-scheme g-C$_3$N$_4$–TiO$_2$ photocatalysts for the decomposition of formaldehyde in air. *Phys. Chem. Chem. Phys.* **2013**, *15*, 16883–16890. [CrossRef]

59. Idrees, F.; Dillert, R.; Bahnemann, D.W.; Butt, F.K.; Tahir, M. In-situ synthesis of Nb$_2$O$_5$/g-C$_3$N$_4$ heterostructures as highly efficient photocatalysts for molecular H$_2$ evolution under solar illumination. *Catalysts* **2019**, *9*, 169. [CrossRef]

60. Di, T.; Xu, Q.; Ho, W.; Tang, H.; Xiang, Q.; Yu, J. Review on metal sulphide-based z-scheme photocatalysts. *ChemCatChem* **2019**, *11*, 1394–1411. [CrossRef]

61. Kumar, S.G.; Rao, K.S.R.K. Zinc oxide based photocatalysis: Tailoring surface-bulk structure and related interfacial charge carrier dynamics for better environmental applications. *RSC Adv.* **2015**, *5*, 3306–3351. [CrossRef]

62. Ribao, P.; Rivero, M.J.; Ortiz, I. TiO$_2$ structures doped with noble metals and/or graphene oxide to improve the photocatalytic degradation of dichloroacetic acid. *Environ. Sci. Pollut. Res.* **2016**, *24*, 12628–12637. [CrossRef]

63. Capilli, G.; Costamagna, M.; Sordello, F.; Minero, C. Synthesis, characterization and photocatalytic performance of p-type carbon nitride. *Appl. Catal. B: Environ.* **2019**, *242*, 121–131. [CrossRef]

64. Fu, J.; Xu, Q.; Low, J.; Jiang, C.; Yu, J. Ultrathin 2D/2D WO$_3$/g-C$_3$N$_4$ step-scheme H2-production photocatalyst. *Appl. Catal. B Environ.* **2019**, *243*, 556–565. [CrossRef]

65. Ye, R.; Fang, H.; Zheng, Y.Z.; Li, N.; Wang, Y.; Tao, X. Fabrication of CoTiO$_3$/g-C$_3$N$_4$ hybrid photocatalysts with enhanced H2 evolution: Z-scheme photocatalytic mechanism insight. *ACS Appl. Mater. Interfaces* **2016**, *8*, 13879–13889. [CrossRef] [PubMed]

66. Da Silva, G.T.; Carvalho, K.T.G.; Lopes, O.F.; Ribeiro, C. g-C$_3$N$_4$/Nb$_2$O$_5$ heterostructures tailored by sonochemical synthesis: Enhanced photocatalytic performance in oxidation of emerging pollutants driven by visible radiation. *Appl. Catal. B Environ.* **2017**, *216*, 70–79. [CrossRef]

67. Wang, W.; Fang, J.; Shao, S.; Lai, M.; Lu, C. Compact and uniform TiO$_2$@g-C$_3$N$_4$ core-shell quantum heterojunction for photocatalytic degradation of tetracycline antibiotics. *Appl. Catal. B Environ.* **2017**, *217*, 57–64. [CrossRef]

68. Jiang, W.; Zong, X.; An, L.; Hua, S.; Miao, X.; Luan, S.; Wen, Y.; Tao, F.F.; Sun, Z. Consciously constructing heterojunction or direct Z-scheme photocatalysts by regulating electron flow direction. *ACS Catal.* **2018**, *8*, 2209–2217. [CrossRef]

69. Hu, X.; Lu, S.; Tian, J.; Wei, N.; Song, X.; Wang, X.; Cui, H. The selective deposition of MoS$_2$ nanosheets onto (101) facets of TiO$_2$ nanosheets with exposed (001) facets and their enhanced photocatalytic H$_2$ production. *Appl. Catal. B Environ.* **2019**, *241*, 329–337. [CrossRef]

70. Isimjan, T.T.; Rasul, S.; Aloufi, M.N.; Khan, M.A.; Alhowaish, I.K.; Ahmed, T. Rational design of Pd-TiO$_2$/g-C$_3$N$_4$ heterojunction with enhanced photocatalytic activity through interfacial charge transfer. *Clean Energy* **2019**, *3*, 59–68. [CrossRef]

71. Liu, J.; Yan, X.T.; Qin, X.S.; Wu, S.J.; Zhao, H.; Yu, W.B.; Chen, L.H.; Liu, J.; Su, B.L.; Si-Jia, W.; et al. Light-assisted preparation of heterostructured g-C$_3$N$_4$/ZnO nanorods arrays for enhanced photocatalytic hydrogen performance. *Catal. Today* **2019**, 1–5. [CrossRef]

72. Liu, C.; Dong, S.; Chen, Y. Enhancement of visible-light-driven photocatalytic activity of carbon plane/g-C$_3$N$_4$/TiO$_2$ nanocomposite by improving heterojunction contact. *Chem. Eng. J.* **2019**, *371*, 706–718. [CrossRef]

73. Wang, J.; Wang, G.; Wang, X.; Wu, Y.; Su, Y.; Tang, H. 3D/2D direct Z-scheme heterojunctions of hierarchical TiO$_2$ microflowers/g-C$_3$N$_4$ nanosheets with enhanced charge carrier separation for photocatalytic H$_2$ evolution. *Carbon* **2019**, *149*, 618–626. [CrossRef]

74. Yuan, N.; Zhang, J.; Zhang, S.; Chen, G.; Meng, S.; Fan, Y.; Zheng, X.; Chen, S. What is the transfer mechanism of photoexcited charge carriers for g-C$_3$N$_4$/TiO$_2$ heterojunction photocatalysts? Verification of the relative p–n junction theory. *J. Phys. Chem. C* **2020**, *124*, 8561–8575. [CrossRef]

75. Li, D.; Wang, S.; Wang, J.; Zhang, X.; Liu, S. Synthesis of CdTe/TiO$_2$ nanoparticles and their photocatalytic activity. *Mater. Res. Bull.* **2013**, *48*, 4283–4286. [CrossRef]

76. Chen, L.; Zhou, X.; Jin, B.; Luo, J.; Xu, X.; Zhang, L.; Hong, Y. Heterojunctions in g-C$_3$N$_4$/B-TiO$_2$ nanosheets with exposed {001} plane and enhanced visible-light photocatalytic activities. *Int. J. Hydrog. Energy* **2016**, *41*, 7292–7300. [CrossRef]

77.　Jo, W.K.; Selvam, N.C.S.; Adinaveen, T.; Vijaya, J.J. Synthesis of MoS_2 nanosheet supported Z-scheme TiO_2 /g-C_3N_4 photocatalysts for the enhanced photocatalytic degradation of organic water pollutants. *RSC Adv.* **2016**, *6*, 10487–10497. [CrossRef]

78.　Huang, S.; Zhong, J.; Li, J.; Chen, J.; Xiang, Z.; Hu, W.; Li, M. Z-scheme TiO_2/g-C_3N_4 composites with improved solar-driven photocatalytic performance deriving from remarkably efficient separation of photo-generated charge pairs. *Mater. Res. Bull.* **2016**, *84*, 65–70. [CrossRef]

79.　Fujihara, K.; Izumi, S.; Ohno, T.; Matsumura, M. Time-resolved photoluminescence of particulate TiO_2 photocatalysts suspended in aqueous solutions. *J. Photochem. Photobiol. A Chem.* **2000**, *132*, 99–104. [CrossRef]

80.　LiQiang, J.; Yichun, Q.; Baiqi, W.; Shudan, L.; Baojiang, J.; Libin, Y.; Wei, F.; Honggang, F.; Jiazhong, S. Review of photoluminescence performance of nano-sized semiconductor materials and its relationships with photocatalytic activity. *Sol. Energy Mater. Sol. Cells* **2006**, *90*, 1773–1787. [CrossRef]

81.　Kubelka, P.; Munk, F. An article on optics of paint layers. *Fuer Tekn. Physik* **1931**, *12*, 593–609.

82.　Murphy, A.B. Band-gap determination from diffuse reflectance measurements of semiconductor films, and application to photoelectrochemical water-splitting. *Sol. Energy Mater. Sol. Cells* **2007**, *91*, 1326–1337. [CrossRef]

83.　Liu, Y.; Zeng, X.; Hu, X.; Hu, J.; Wang, Z.; Yin, Y.; Sun, C.; Zhang, X. Two-dimensional g-C_3N_4/TiO_2 nanocomposites as vertical Z-scheme heterojunction for improved photocatalytic water disinfection. *Catal. Today* **2019**, *335*, 243–251. [CrossRef]

84.　Lin, X.; Xing, J.; Wang, W.; Shan, Z.; Xu, F.; Huang, F. Photocatalytic activities of heterojunction semiconductors Bi_2O_3/$BaTiO_3$: A strategy for the design of efficient combined photocatalysts. *J. Phys. Chem. C* **2007**, *111*, 18288–18293. [CrossRef]

85.　Christoforidis, K.C.; Sengele, A.; Keller, V.; Keller, N. Single-step synthesis of SnS_2 nanosheet-decorated TiO_2 anatase nanofibers as efficient photocatalysts for the degradation of gas-phase diethylsulfide. *ACS Appl. Mater. Interfaces* **2015**, *7*, 19324–19334. [CrossRef] [PubMed]

86.　Shang, Y.; Chen, X.; Liu, W.; Tan, P.; Chen, H.; Wu, L.; Ma, C.; Xiong, X.; Pan, J. Photocorrosion inhibition and high-efficiency photoactivity of porous g-C_3N_4/Ag_2CrO_4 composites by simple microemulsion-assisted co-precipitation method. *Appl. Catal. B Environ.* **2017**, *204*, 78–88. [CrossRef]

87.　Maheu, C.; Cardenas, L.; Puzenat, E.; Afanasiev, P.; Geantet, C. UPS and UV spectroscopies combined to position the energy levels of TiO_2 anatase and rutile nanopowders. *Phys. Chem. Chem. Phys.* **2018**, *20*, 25629–25637. [CrossRef]

88.　Ong, W.J.; Putri, L.K.; Tan, L.L.; Li, N.; Ng, Y.H.; Wen, X.; Chai, S.P. Unravelling charge carrier dynamics in protonated g-C_3N_4 interfaced with carbon nanodots as co-catalysts toward enhanced photocatalytic CO_2 reduction: A combined experimental and first-principles DFT study. *Nano Res.* **2017**, *10*, 1673–1696. [CrossRef]

89.　Low, J.; Dai, B.; Tong, T.; Jiang, C.; Yu, J. In situ irradiated X-ray photoelectron spectroscopy investigation on a direct Z-scheme TiO_2/CdS composite film photocatalyst. *Adv. Mater.* **2018**, *31*, e1802981. [CrossRef]

90.　Fernández-Castro, P.; Vallejo, M.; Román, M.F.S.; Ortiz, I. Insight on the fundamentals of advanced oxidation processes. Role and review of the determination methods of reactive oxygen species. *J. Chem. Technol. Biotechnol.* **2015**, *90*, 796–820. [CrossRef]

91.　Ribao, P.; Corredor, J.; Rivero, M.J.; Ortiz, I. Role of reactive oxygen species on the activity of noble metal-doped TiO_2 photocatalysts. *J. Hazard. Mater.* **2019**, *372*, 45–51. [CrossRef]

92.　Christoforidis, K.C.; Montini, T.; Bontempi, E.; Zafeiratos, S.; Jaén, J.J.D.; Fornasiero, P. Synthesis and photocatalytic application of visible-light active β -Fe_2O_3 /g-C_3N_4 hybrid nanocomposites. *Appl. Catal. B Environ.* **2016**, *187*, 171–180. [CrossRef]

93.　Jia, X.; Tahir, M.; Pan, L.; Huang, Z.F.; Zhang, X.; Wang, L.; Zou, J.J. Direct Z-scheme composite of CdS and oxygen-defected $CdWO_4$: An efficient visible-light-driven photocatalyst for hydrogen evolution. *Appl. Catal. B Environ.* **2016**, *198*, 154–161. [CrossRef]

94.　Cui, H.; Li, B.; Zhang, Y.; Zheng, X.; Li, X.; Li, Z.; Xu, S. Constructing Z-scheme based $CoWO_4$/CdS photocatalysts with enhanced dye degradation and H_2 generation performance. *Int. J. Hydrog. Energy* **2018**, *43*, 18242–18252. [CrossRef]

95.　Obregón, S.; Ruíz-Gómez, M.; Rodríguez-González, V.; Vázquez, A.; Hernández-Uresti, D. A novel type-II $Bi_2W_2O_9$/g-C_3N_4 heterojunction with enhanced photocatalytic performance under simulated solar irradiation. *Mater. Sci. Semicond. Process.* **2020**, *113*, 105056. [CrossRef]

96. Huang, Z.; Sun, Q.; Lv, K.; Zhang, Z.; Li, M.; Li, B. Effect of contact interface between TiO_2 and g-C_3N_4 on the photoreactivity of g-C_3N_4/TiO_2 photocatalyst: (001) vs (101) facets of TiO_2. *Appl. Catal. B Environ.* **2015**, *164*, 420–427. [CrossRef]

97. Meng, A.; Zhu, B.; Zhong, B.; Zhang, L.; Cheng, B. Direct Z-scheme TiO_2/CdS hierarchical photocatalyst for enhanced photocatalytic H_2-production activity. *Appl. Surf. Sci.* **2017**, *422*, 518–527. [CrossRef]

98. Wang, S.; Zhu, B.; Liu, M.; Zhang, L.; Yu, J.; Zhou, M. Direct Z-scheme ZnO/CdS hierarchical photocatalyst for enhanced photocatalytic H_2-production activity. *Appl. Catal. B Environ.* **2019**, *243*, 19–26. [CrossRef]

99. Han, C.; Likodimos, V.; Khan, J.A.; Nadagouda, M.N.; Andersen, J.; Falaras, P.; Rosales-Lombardi, P.; Dionysiou, D.D. UV–visible light-activated Ag-decorated, monodisperse TiO_2 aggregates for treatment of the pharmaceutical oxytetracycline. *Environ. Sci. Pollut. Res.* **2013**, *21*, 11781–11793. [CrossRef]

100. Dvoranová, D.; Barbieriková, Z.; Brezová, V. Radical intermediates in photoinduced reactions on TiO_2 (An EPR spin trapping study). *Molecules* **2014**, *19*, 17279–17304. [CrossRef]

101. Kim, M.; Kim, Y.K.; Lim, S.K.; Kim, S.; In, S.I. Efficient visible light-induced H_2 production by Au@CdS/TiO_2 nanofibers: Synergistic effect of core–shell structured Au@CdS and densely packed TiO_2 nanoparticles. *Appl. Catal. B Environ.* **2015**, *166*, 423–431. [CrossRef]

102. Tan, Y.; Shu, Z.; Zhou, J.; Li, T.; Wang, W.; Zhao, Z. One-step synthesis of nanostructured g-C_3N_4/TiO_2 composite for highly enhanced visible-light photocatalytic H_2 evolution. *Appl. Catal. B Environ.* **2018**, *230*, 260–268. [CrossRef]

103. Luo, Y.; Deng, B.; Pu, Y.; Liu, A.; Wang, J.; Ma, K.; Gao, F.; Gao, B.; Zou, W.; Dong, L. Interfacial coupling effects in g-C_3N_4/$SrTiO_3$ nanocomposites with enhanced H_2 evolution under visible light irradiation. *Appl. Catal. B Environ.* **2019**, *247*, 1–9. [CrossRef]

104. Hao, R.; Wang, G.; Jiang, C.; Tang, H.; Xu, Q. In situ hydrothermal synthesis of g-C_3N_4/TiO_2 heterojunction photocatalysts with high specific surface area for Rhodamine B degradation. *Appl. Surf. Sci.* **2017**, *411*, 400–410. [CrossRef]

105. Zhou, F.Q.; Fan, J.; Xu, Q.J.; Min, Y.L. $BiVO_4$ nanowires decorated with CdS nanoparticles as Z-scheme photocatalyst with enhanced H_2 generation. *Appl. Catal. B Environ.* **2017**, *201*, 77–83. [CrossRef]

106. Jin, J.; Yu, J.; Guo, D.; Cui, C.; Ho, W. A hierarchical z-scheme CdS-WO_3 photocatalyst with enhanced CO_2 reduction activity. *Small* **2015**, *11*, 5262–5271. [CrossRef]

107. Jiang, Z.; Wan, W.; Li, H.; Yuan, S.; Zhao, H.; Wong, P.K. A hierarchical Z-scheme α-Fe_2O_3/g-C_3N_4 hybrid for enhanced photocatalytic CO_2 reduction. *Adv. Mater.* **2018**, *30*, 1706108. [CrossRef]

108. Raziq, F.; Li, C.; Humayun, M.; Qu, Y.; Zada, A.; Yu, H.; Jing, L. Synthesis of TiO_2/g-C_3N_4 nanocomposites as efficient photocatalysts dependent on the enhanced photogenerated charge separation. *Mater. Res. Bull.* **2015**, *70*, 494–499. [CrossRef]

109. Zhang, J.; Qiao, S.Z.; Qi, L.; Yu, J. Fabrication of NiS modified CdS nanorod p–n junction photocatalysts with enhanced visible-light photocatalytic H_2-production activity. *Phys. Chem. Chem. Phys.* **2013**, *15*, 12088–12094. [CrossRef]

110. Wang, M.; Xiong, H.; Hu, Y.; Han, J.; Rong, G.; Yin, Y. TiO_2/NiO hybrid shells: P–n junction photocatalysts with enhanced activity under visible light. *J. Mater. Chem. A* **2015**, *3*, 20727–20735. [CrossRef]

111. Uddin, T.; Nicolas, Y.; Olivier, C.; Jaegermann, W.; Rockstroh, N.; Junge, H.; Toupance, T. Band alignment investigations of heterostructure NiO/TiO_2 nanomaterials used as efficient heterojunction earth-abundant metal oxide photocatalysts for hydrogen production. *Phys. Chem. Chem. Phys.* **2017**, *19*, 19279–19288. [CrossRef]